Design of multi-junction solar cells based on thin film silicon

H. Parasramka

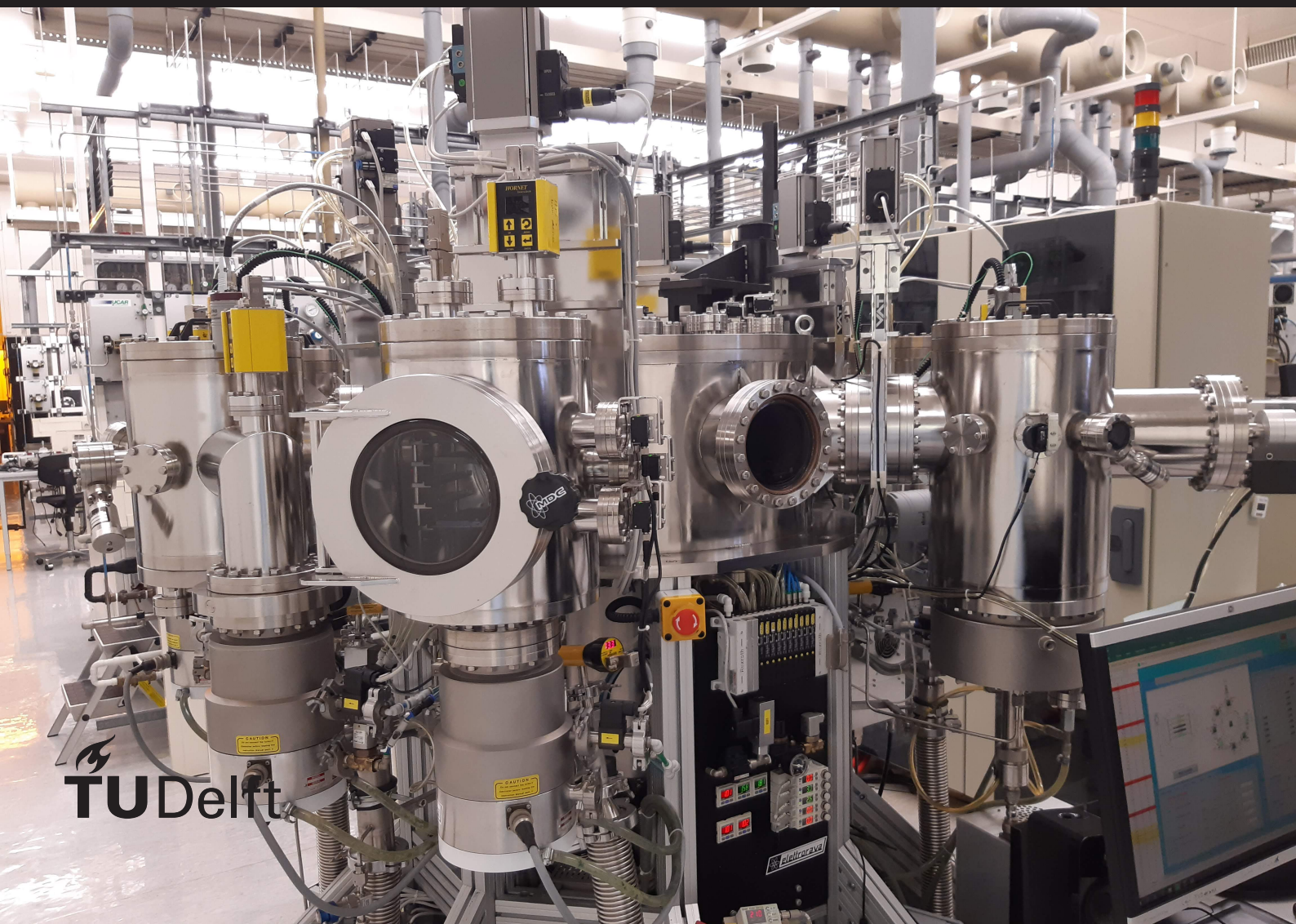

TU Delft

Design of multijunction solar cells based on thin film silicon

by

H. Parasramka

to obtain the degree of Master of Science
at the Delft University of Technology,
to be defended publicly on Wednesday July 22, 2020 at 9:30 AM.

Student number:	4840534	
Project duration:	October 21, 2019 – July 22, 2020	
Thesis committee:	Prof. dr. ir. A.H.M. Smets,	TU Delft, supervisor
	Dr. ir. R. Santbergen,	TU Delft, Assistant Professor
	Dr. ir. G. R. Chandra Mouli	TU Delft, Assistant Professor
	Ir. T. de Vrijer,	Ph.D. candidate (TU Delft), daily supervisor

TU Delft

”What I cannot create, I do not understand.”

Richard P. Feynman

Preface

This report presents the work done on the thesis project titled 'Design of multijunction solar cells based on thin film silicon.' This thesis was completed to fulfill the requirements of a Master of Science degree in Sustainable Energy Technology at TU Delft. I was engaged in this project from late October 2019 till July 2020.

In chapter 1, I have attempted to motivate this thesis in the broader context of solar photovoltaics. The theoretical background necessary to interpret the work done is presented in chapter 2. A large amount of the work is based on experimental results, and an explanation of the experimental methods is provided in chapter 3. Chapters 4 through 6 discuss the results obtained, and the conclusions are presented in chapter 7.

I would like to take this opportunity to thank everyone who has helped me during this period. Firstly, I would like to thank my daily supervisor Thierry de Vrijer for his guidance, good cheer, and faith in me. I would also like to thank Prof. Arno Smets for his insightful feedback and generosity of spirit. I would like to mention my research partner David van Nijen for being a true team player. Special thanks go to Martijn Tijssen for taking care of problems with the cleanroom equipment, and Remko Koornneef for ensuring that the measurement equipment was reliable. I would also like to thank Dr. Rudi Santbergen for answering my questions related to GENPRO4. These past few months have shown me the value of working collaboratively; and I am grateful to everyone in the PVMD group for this experience.

Finally, I thank my parents for their unwavering love and support, without which not much would be possible.

H. Parasramka
Delft, July 2020

Contents

1

Introduction

In 2019, solar PV continued its steady march around our increasingly sustainable ”pale blue dot” [39]. A record-breaking 115 GW of solar had been installed last year, resulting in a cumulative global capacity of 627 GW [38]. Although the novel coronavirus pandemic has interrupted supply chains and frustrated deployment, the case for solar energy remains strong [33].

An overwhelming majority of the commercially available PV modules are based on crystalline silicon. There are several reasons for this. Firstly, silicon is among the most abundant elements on the planet and thus easily available. Secondly, its electronic properties make it particularly suited to harness the incoming light from the sun. Specifically, its bandgap minimizes the losses that occur in solar cells due to spectral mismatch (these terms are explained in later chapters). These advantages made the silicon a prime candidate for the initial development of solar cells. Over time, research efforts have pushed the efficiency of this technology from around 13% in the late 1970s to more than 26% as of this year [22]. A compelling reason for the widespread use of crystalline silicon is its low prices. Economies of scale have allowed the prices to drop from more than 50 $ per W in 1976 to around 0.40 $ per W in 2018 (in terms of 2017 $) [16]. Particularly in recent years, the prices have dropped steeply owing to rapid upscaling of manufacturing in China. Thus, due to a combination of technological suitability, research efforts, policy support and economies of scale, crystalline silicon is now the primary technology for commercial PV modules.

An alternative to crystalline silicon is amorphous silicon and its alloys, also referred to as thin film silicon. The material is cheap, lightweight, performs better than crystalline silicon at higher temperatures, and can be deposited on flexible substrates [36]. An important challenge with thin film silicon is its low efficiency, which deteriorates (reversibly) when exposed to light. Due to this technological limitation, the global market share of thin film silicon was less than 1% as of 2017 [16]. However, in places where thin film silicon continues to be used, it is not easily replaceable by crystalline silicon. Thin film silicon modules are lighter and can be made flexible. They can thus be installed safely and economically over buildings with weak or curved roofs, unlike glass-based crystalline silicon modules which are rigid and heavy. Furthermore, flexible thin film silicon modules can be simply rolled out on the ground with minimal costs associated with the ”balance of system”. Layers of thin film silicon are also used together with crystalline silicon to yield a high efficiency ”heterojunction” device. The HIT modules sold by Panasonic are based on such a technology. Thus, despite its limitations, thin film silicon has unique advantages which make it particularly suitable for niche applications.

The objective of this thesis is to contribute to the design of multijunction solar cells based on thin film silicon alloys. A possible valuable application of such a device is in a solar-to-fuel device. The basic function of such a device is to convert water and CO_2 to hydrogen and carbon monoxide using energy from the sun. While such a device may be built solely with crystalline silicon cells, thin film silicon offers unique advantages such as greater flexibility in operating voltage, fewer cell interconnections, and integrated applications. Thus, it is important to firmly establish ways of optimizing such a multijunction photovoltaic device because it may uncover a route to clean fuels.

The aforementioned goal is divided into 3 research objectives. The first research objective is to develop a high V_{OC} top junction. Optimizing the top junction is important because it can increase the total V_{OC} from the whole device and it affects the light reaching the underlying junctions. The second research objective is the optimal design of a-SiGe based cells. a-SiGe based cells are highly versatile, and an optimal way of designing them can result in more efficient multijunctions. The final research objective was to optimize the tunnel recombination junctions (TRJs). TRJs are among the most complex and vital parts of multijunctions, and a better understanding of their behaviour can contribute to a better performing device. These 3 research questions are respectively addressed in chapters 4, 5, and 6. The conclusions stemming from the work done are finally discussed in chapter 7.

2

Theoretical background

The objective of this chapter is to provide the theoretical framework for the rest of the document. Most of the results presented in this report will be discussed in terms of the band theory of solids. This model is introduced in section 2.1. This is followed by a note on some unique features of the band diagram of amorphous silicon, and the consequences these features have on device performance. The topic of doping, which is essential for working solar cells, is presented next. Finally, the behaviour of basic photovoltaic devices is addressed briefly.

2.1. Band theory of solids

Band diagrams are used to visualize the generation and movement of charge carriers in solids. This can be qualitatively motivated as follows (based on the explanation given in [30]). Electrons in atoms can only exist in discrete energy levels. When two similar atoms are brought close to each other, the energy levels of the outermost electrons in the two atoms begin to overlap and interact with each other. The result of this interaction is the splitting of the energy level into two. This behaviour is consistent with the Pauli exclusion principle, which states that no two electrons can occupy the same quantum state.

If N atoms are brought together to form a solid, a single energy level would split into N energy levels. The distance (or difference in energy) between adjacent levels is in the order of $1/N$. As N becomes very large, the distance between adjacent levels becomes very small. For instance, 14 grams of silicon will have $6.022x10^{23}$ atoms. The distance between adjacent energy levels would then be in the order of $10^{-24}eV$, which is negligibly small [30]. In this way, a discrete energy level in a single atom becomes a quasi-continuous band of energy levels in a solid.

The electrons furthest away from the nucleus, while still being bound to the atom, are known as valence electrons. The splitting of their energy levels leads to the formation of the valence band. Above the valence band, there is a band of forbidden energy levels which cannot be occupied by electrons. This forbidden band is a consequence of the fact that energy levels in atoms are discretized; and some energy levels are simply not accessible to electrons. Above the forbidden gap is the conduction band, which corresponds to the energy levels of excited electrons. These electrons are no longer bound to their nuclei and are free to travel through the solid. As shown in Figure 2.1, the band diagrams of metals, semiconductors, and insulators are represented differently in order to convey differences in their observed behaviour. Metallic solids are conductors. Their valence electrons are already in a conducting state at room temperature in the dark. In terms of the band diagram, the valence and conduction bands overlap in a metal and there is no forbidden gap. Semiconductors and insulators do not conduct electricity at room temperature in the dark, and thus their band diagrams shows a forbidden gap (also known as a bandgap). If a semiconductor is exposed to certain wavelengths of light, an electron in the valence band can absorb the energy of the incoming photon and jump into the conduction band. Insulators do no share this feature. This difference in behaviour is expressed in the form of a wider forbidden gap in insulators. In addition to the energy bands, Figure 2.1 also shows the

Fermi energy level. This can be understood to represent the average energy level of the electrons in the solid.

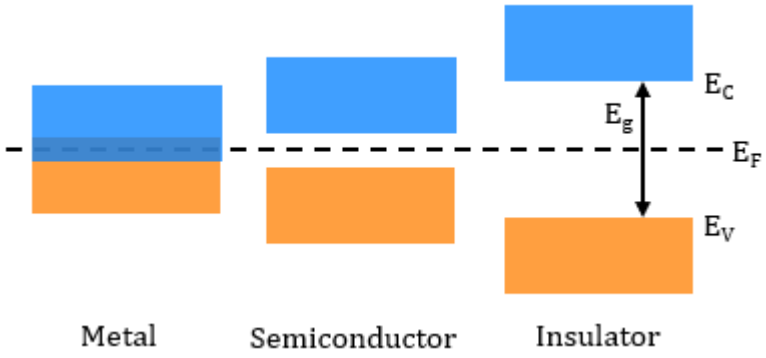

Figure 2.1: The band diagram representation of metals, semiconductors, and insulators. E_C and E_V represent the edges of the conduction and valence bands respectively. E_g is the bandgap, or the width of the forbidden band. E_F is the Fermi energy level, and is taken to mean the average potential energy of the electrons.

2.2. Special note on the structure of amorphous silicon

In the band diagram of a semiconductor shown in Figure 2.1, the energy bands are shown to have well-defined edges. This description only applies to semiconductors whose lattices show ”long range order”, such as crystalline silicon. A lattice is said to possess long-range order if it can be described as a set of identical unit cells which are stacked close to each other. The bond lengths and angles remain the same throughout the silicon crystal. Consequently the energy required to break a given bond (and obtain a free electron) does not vary. Equivalently, crystalline silicon can be described as having a well-defined bandgap, as represented in Figure 2.1.

The structure of amorphous silicon, however, is markedly different. It has conventionally been described as a continuous random network (CRN), in which the silicon matrix has short-range order (the atoms still possess tetrahedral shapes) but lack long range order [36]. The angles between different bonds, and the lengths of the bonds, are distorted. These distortions lead to a number of dangling bonds as well, which are valence electrons that do not form part of a covalent bond with a neighbouring atom. In the CRN model, these dangling bonds have been described as the dominant defect in amorphous silicon. Recent evidence, however, points us towards an anisotropic disordered network (ADN) model. This theory suggests that dangling bonds tend to agglomerate inside the amorphous material, and the resulting volume deficiencies exert more influence over the material’s properties than isotropically distributed dangling bonds [26]. In sum, amorphous silicon is best described as a matrix of distorted Si-Si bonds with defects in the form of agglomerated vacancies and voids.

The defects in the amorphous silicon material have important consequences for its band diagram. Firstly, the electron wave exhibits diffraction whenever it encounters defects inside the material. When the degree of disorder is sufficiently high, the electron becomes a standing wave confined to a localized energy state [23]. In other words, the disorder in the material leads to the creation of localized energy states not available in the crystalline lattice. These localized states are called ”band tails” and populate the region close to the conduction and valence band edges. Secondly, the dangling bonds themselves offer additional energy states inside the forbidden gap which electrons can then occupy. The net effect of these additional energy states is that the amorphous silicon band diagram should not be shown to have sharp conduction and valence band edges. Instead, the bands should give way to band tail states which decay exponentially into the bandgap, and additional defect states in the forbidden gap due to the dangling bonds [35].

This picture of amorphous silicon raises questions regarding the physical meaning of its so-called ”bandgap”. If electrons can occupy energy states below the conduction band edge and above the

valence band edge, where is the band ”gap”? There is no single answer to this question. Several definitions of bandgap exist. In this report, the ”iso-absorption bandgap” is used. Symbolically represented as E_{04}, this term refers to the photon energy at which the absorption coefficient equals $10^4 cm^{-1}$.

Upto this point, electrons have been presented as waves. The interference of a large number of neighbouring electron waves leads to the creation of bands; and the diffraction of electron waves inside a sufficiently imperfect crystal leads to the localized tail states in amorphous silicon. From the next section onward, the discussion revolves around photovoltaic devices. In that context, it is more useful to fall back on the intuitive idea of electron ”particles” and set aside the wave nature of electrons.

2.3. Charge carriers and doping

When a semiconductor is exposed to light, a valence electron may interact with a sufficiently energetic photon and leap up to the conduction band, leaving behind a ”hole” in the valence band. A large number of such absorption events may occur, resulting in a large number of electrons and holes in the conduction and valence bands respectively. Under the influence of an electric field, all electrons drift in the opposite direction of the applied field. In the valence band, electrons drift by moving to occupy the nearest holes, leaving behind holes in their old places. These holes are in turn occupied by other electrons, which also leave behind holes, and so on. Equivalently, drift in the valence band can be visualized as the movement of a hypothetical, positively charged hole in the direction of the electric field. Thus, there are two types of charge carriers in semiconductors - electrons which carry negative charge in the conduction band, and holes which carry positive charge in the valence band.

In pure silicon, there are as many holes as there are electrons. For applications in photovoltaics, the relative concentrations of electrons and holes is adjusted by adding carefully chosen impurities. This process is called ”doping”. Doping can either be of ”p-type” or ”n-type” depending on the specific impurity added.

P-type doping involves adding a group III element, usually boron, to silicon. Silicon has 4 valence electrons, each of which contributes to a covalent bond with a neighbouring silicon atom in a pure silicon crystal. When boron is added, it replaces some of the silicon atoms in the lattice. It has 3 valence electrons, each of which may be contributing to a covalent bond with a neighbouring silicon atom. However, the lack of a fourth valence electron means that, in effect, a hole is created. Thus, the addition of group III elements like boron in the silicon lattice leads to an excess of holes, which are positively charge carriers. This is why this is called p-type doping. In n-type doping, a group V element such as phosphorous is used create excess electrons. Phosphorous has 5 valence electrons. In the silicon lattice, 4 of these electrons will contribute to covalent bonds but the fifth electron is unbound. This excess electron carries negative charge in the conduction band. In the following section, it will be shown how the effects of doping can be leveraged to develop devices which can harness the sun’s energy.

2.4. The P-I-N junction

Electrons and holes may travel through a semiconductor through two possible mechanisms - drift and diffusion. Drift refers to the motion of a charge carrier in response to an applied electric field, and diffusion is the movement resulting from a concentration gradient. The diffusion of charge carriers is limited by their ”diffusion length”, a parameter which may be interpreted as the typical distance a carrier diffuses before it recombines with a particle of opposite charge, effectively being annihilated. Diffusion lengths are very small in a defective material such as amorphous silicon. Hence, carrier transport in these cells cannot be done via diffusion and must rely on drift current. In order to realize such a drift device, an intrinsic or undoped semiconductor layer is sandwiched between a p-layer and an n-layer. This is the p-i-n junction.

Figure 2.2 shows the band diagrams of the 3 layers of a p-i-n junction which are not in contact with each other. The Fermi level is close to the valence band in the p-layer, close to the conduction band in the n-layer, and nearly equidistant from both band edges in the i-layer. When these layers are brought into contact, the Fermi levels across these layers must be the same. This is because the Fermi

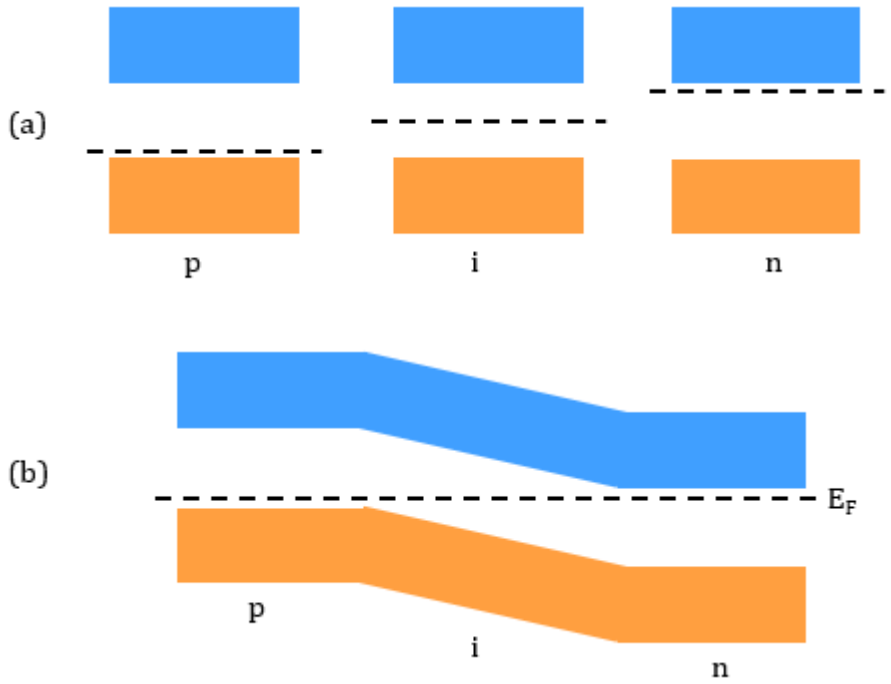

Figure 2.2: (a) Band diagrams of p-doped, intrinsic, and n-doped layers not placed in contact (b) Band diagram of a p-i-n solar cell.

level represents the average potential of the electrons, and the potential across the device must remain constant in equilibrium. Furthermore, the conduction and valence band edges must remain continuous. As a result of these two constraints and the influence of doping, the conduction and valence bands in the intrinsic layer bend. The slope of the band edges represents the electric field across the intrinsic layer. In response to this electric field, electrons travel down the slope of the conduction band and are collected at the i/n interface. Holes travel up the slope of the valence band and are collected at the i/p interface. Thus, a net current flows from the n-layer to the p-layer. This is how a basic thin film silicon solar cell operates.

3

Experimental and simulation details

The objective of this chapter is to explain the research methods used for this project. First, the basic structure of thin film silicon solar cells is outlined. This is followed by a section on the processing techniques used to build these solar cells. Section 3.2 discusses the methods used to characterise the performance of solar cells and thin films. Simulation work was done to complement the experimental results and the relevant software tools are described in section 3.4.

An image of a thin film silicon solar cell, as processed on textured glass in the lab at TU Delft, is shown in Figure 3.1. To give a better idea of the layers constituting the solar cell, an exploded view is shown in Figure 3.2. The incident light generates charge carriers in the intrinsic layer, where the built-in electric field causes holes to drift towards the p-layer and electrons to drift towards the n-layer. In order for these charge carriers to contribute electric current, they need to reach an external circuit. For this, transparent conductive oxides or TCOs are used on either side of the p-i-n junction. Holes are collected at the front TCO which is indium tin oxide (ITO). This layer also helps promote the in-coupling of light into the cell. The TCO at the back is aluminium-doped zinc oxide (AZO) and it collects electrons. After the AZO is deposited on textured glass, two strips of heat-resistant Kapton tape are placed along the edges of the substrate. This shields the AZO from the deposition of all subsequent layers. The tape is finally removed and the AZO can be used as the negative terminal of the cell. A metallic contact placed in front of the ITO acts as the positive terminal.

From Figure 3.1, it can be seen that each substrate actually has several, separate ITO films on its surface and each such ”dot” has its own metallic contact. Multiple dots are processed, and measured, for each substrate in order to improve the reliability of the measurement.

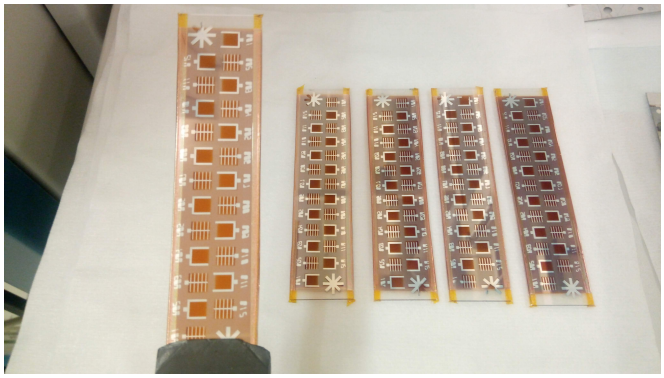

Figure 3.1: Image of a set of thin film silicon cells produced for this thesis in the Else Kooi Lab at TU Delft.

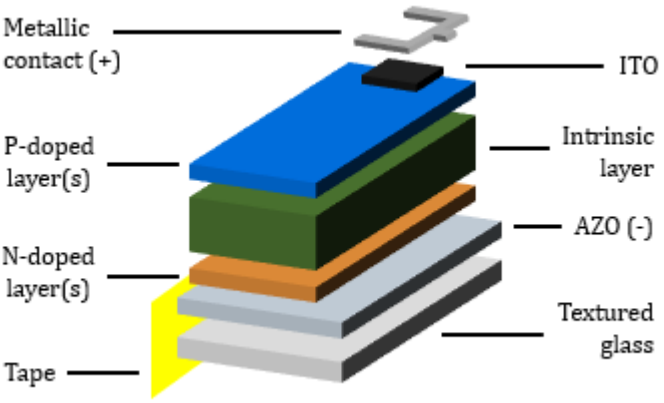

Figure 3.2: An exploded view of a single junction solar cell deposited in n-i-p configuration. The dimensions are not to scale. Tape is used on both sides of the substrate but shown only on one side in the figure for clarity. The arrow indicates the direction of incident light.

3.1. Processing techniques

As shown in Figure 3.2, the cells deposited for this thesis were in n-i-p substrate configuration. This means that the n-layer is deposited before the i-layer, which in turn is deposited before the p-layer. The cell configuration, and deposition sequence, have important consequences for cell performance which become apparent in later chapters.

There are five main steps involved in the deposition of n-i-p thin film solar cells. In order, these are:

1. Substrate preparation
2. Sputtering of back TCO
3. Chemical vapour deposition of doped and intrinsic layers
4. Sputtering of front TCO
5. Electron beam evaporation of front metal contact

All of the processing steps mentioned above were done in the Cleanroom 10000 of the Else Kooi Lab at TU Delft. The conditions in the cleanroom are maintained such that there are at most 10000 particles larger than 0.5 micron per cubic feet. Thin films are processed in this environment in order to minimize the intrusion of undesirable impurities.

After completing the aforementioned steps, the cells are annealed at 130°C for 30 minutes in order to improve contact adhesion between the cell and the metal contact. In the following subsections, the processing techniques are described in detail.

3.1.1. Substrate preparation

The substrate refers to the base on top of which the cell or film is deposited. Solar cells were processed on clean, textured glass. Flat pieces of glass were cleaned by immersing them for 10 minutes each in an ultrasonic acetone bath followed by an ultrasonic isopropyl alcohol (IPA) bath. The glass was dried completely using a N_2 gun before any processing takes place. A layer of aluminium doped zinc oxide (AZO) was deposited on the clean glass using radio frequency (RF) magnetron sputtering at 300°C. This layer was etched away using a 1:3:6 solution of 40% hydrofluoric acid (HF), 69% nitric acid (HNO_3) and water, respectively. This gives rise to a textured surface on the glass. This textured glass was cleaned before processing.

3.1.2. Plasma-enhanced chemical vapour deposition (PECVD)

PECVD is a standard process used for the growth of doped and intrinsic thin films. The substrate is placed between two electrodes inside a 300°C reaction chamber which is pumped to vacuum. A mixture of ”precursor gases” is introduced in the chamber. These gases provide the material for the thin films. For instance, the precursor for amorphous silicon films is silane gas. An alternating electric field is created between the two electrodes.The alternating electric field partially ionizes the gas. Energetic electrons collide with other molecules and further dissociate the gas. The resulting ”cloud” of electrons, positive ions, negative ions, and neutral radicals and molecules is called the plasma.

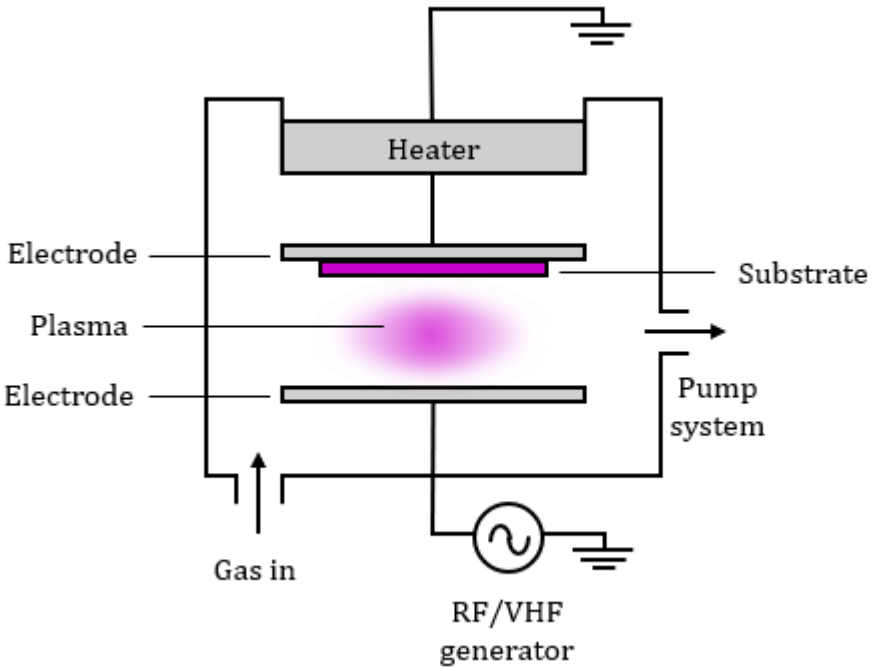

Figure 3.3: A schematic representation of the PE-CVD process in a single reaction chamber.

The growth of thin films occurs in the following manner. Since electrons are much lighter than ions, they undergo a much stronger acceleration in response to the electric field. The result is a net flux of highly mobile electrons towards the substrate [27]. The remaining plasma is positively charged with respect to the substrate. This potential difference drives positively charged ions towards the surface, and traps negative ions within the plasma. With respect to neutral radicals, their concentration is much higher in the plasma as compared to the substrate. This gradient causes neutral radicals to diffuse towards the growth surface [36]. When the alternating electric field is switched off, the remaining plasma returns to a neutral gas state which is pumped out of the chamber. In this manner, positively charged ions and neutral radicals in the plasma contribute to the growth of thin films.

In this thesis, the PECVD cluster tool in the Else Kooi Lab at TU Delft was used for processing. A radio frequency (RF) signal of 13.56MHz was used to create the plasma for the deposition of all layers except for nanocrystalline silicon. For nanocrystalline silicon, a very high frequency (VHF) signal of 40 MHz was used. Separate chambers were used for the deposition of n-doped, intrinsic, and p-doped layers to prevent cross contamination. PECVD results in the growth of thin films not just on the substrate but also on the chamber walls and electrodes [36]. The material along the chamber walls and electrodes can add undesirable impurities in subsequently deposited films. To tackle this, the reaction chambers of the cluster tool at TU Delft are regularly cleaned. Additionally, the chambers were conditioned with the deposition plasma before that plasma was used to grow thin films.

3.1.3. Sputtering

Sputtering is used for the deposition of AZO and ITO. The substrate is placed inside a vacuum chamber. It acts as the anode. The cathode or ”target” is made of the material which is to be deposited. Argon

gas is introduced inside the chamber. An oscillating electric field ionizes the argon gas. Positively charged argon ions bombard the cathode, ejecting atoms of the target material. These atoms diffuse towards the anode and contribute to the deposition of the TCO.

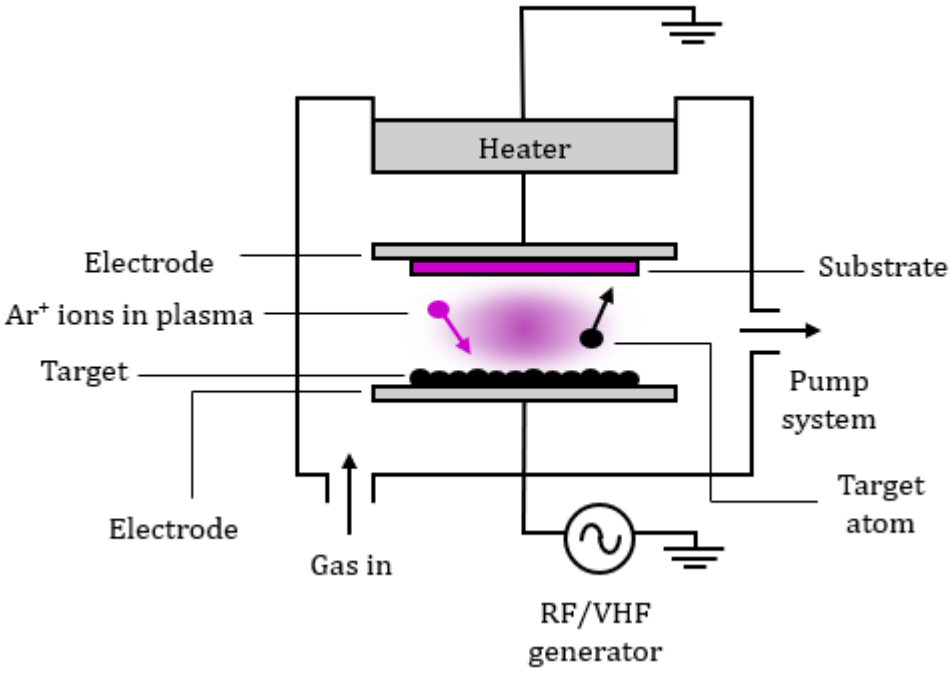

Figure 3.4: A schematic representation of the sputtering process.

3.1.4. Electron beam evaporation

Electron beam evaporation is used for the deposition of aluminium contacts. The substrate is placed in a rotating holder. High purity aluminium is loaded in the crucible. An electron beam, emitted by a tungsten filament, is directed towards the crucible using magnetic fields. The kinetic energy of the beam evaporates the metal. The metallic vapours rise through the chamber and condense on the substrate. Rotating the holder improves the uniformity of the deposition.

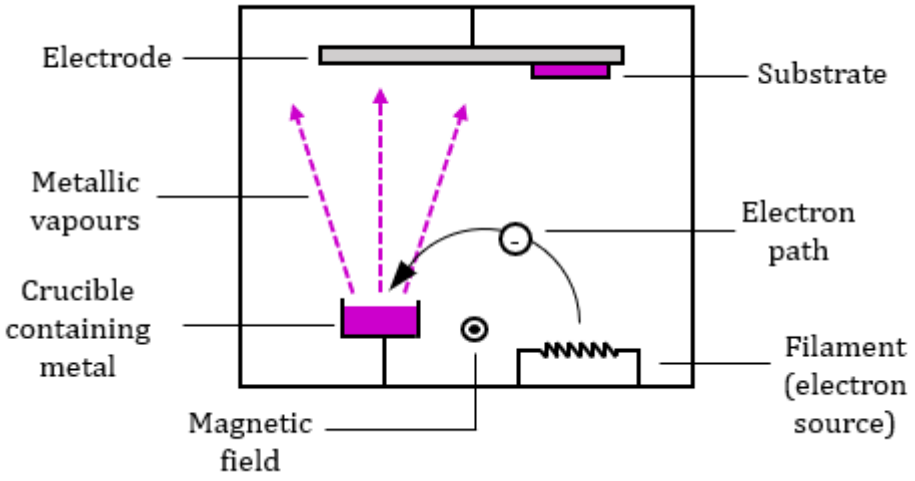

Figure 3.5: A schematic representation of electron beam evaporation.

3.2. Characterization techniques

The previous section describes the methods used to deposit solar cells. An important parameter in these depositions is the deposition time, which affects both the layer thickness and, in some materials, the crystallinity [2]. To estimate the deposition rates of different layers, spectroscopic ellipsometry measurements of different films were carried out. Ellipsometry was also used to measure the complex refractive indices of films, which are necessary for the optical modelling and light management of solar cells. The performance of solar cells was assessed using J-V curves and graphs of external quantum efficiency (EQE). These characterization techniques are detailed in the following subsections.

3.2.1. Spectroscopic ellipsometry

Spectroscopic ellipsometry measurements are used to determine the optical and physical properties of thin films. A thin film on flat glass is placed on a stage. Light of a known polarization obliquely reflects off the film and reaches a detector. The detector measures the change in the polarization of the reflected light. The measurement is carried out at multiple angles of incidence close to the Brewster angle to obtain the maximum difference in the polarization of the reflected light.

The data measured above is subsequently fit to a highly detailed model representing the structure of the thin film. The fitting process is iterated several times and checked manually to find the settings at which the mean square error (MSE) between the model and the data is at its global minimum. Various parameters of this model are then taken to represent the properties of the thin film. These include, but are not limited to, the complex refractive index, thickness, roughness, and bandgap.

3.2.2. J-V curves

The J-V curve of a solar cell is a standard method of assessing its performance. The current density J of the cell is plotted along the y-axis, and the voltage is plotted along the x-axis. The point at which the curve intersects the y-axis gives the short-circuit current density or J_{SC}. The intersection of the J-V curve with the x-axis gives us the open circuit voltage or V_{OC}. At each point of the curve, the product of J and V gives the power per unit area delivered by the cell. The maximum power point is the point in the graph at which the J and V values yield the highest power per unit area. The corresponding current density and voltage values are represented by J_{mp} and V_{mp} respectively. The performance of the cell in short circuit, open circuit, and maximum power conditions are useful indicators of its performance.

Fill factor is an important measure of cell behaviour. It is mathematically defined as follows:

$$FF = \frac{J_{mp}V_{mp}}{J_{sc}V_{oc}}$$

Graphically, the fill factor is an indicator of the ”squareness” of J-V curve. From the above formula, it can be seen that the fill factor can be determined from the J-V curve.

In order to obtain the J-V curve, cells are placed under a solar simulator and maintained at 25°C. Probes are placed on the cell and the voltage is varied from -0.1V to 1V. At each voltage value, the current through the cell is measured. The current can be divided by the area of the cell to yield the current density. This set of values is used to construct the J-V curve.

There are two reasons why the value of J_{SC} as obtained above may be inaccurate. Firstly, there is a mismatch between the AM1.5G spectrum and the spectrum of the solar simulator. The second cause of errors is an inaccurate determination of the active cell area. Thus, the J-V measurement is only used to calculate the V_{OC}, FF, and resistances while the J_{SC} is calculated from the EQE measurement (next section). This approach has been outlined in other papers as well [49].

3.2.3. External quantum efficiency

The external quantum efficiency of a solar cell is the ratio of number of collected charge carriers to the number of incident photons, at each wavelength.

The EQE measurement is done using an in-house setup. The light source is a Xenon lamp. A monochromator is used to obtain photons in a small wavelength range. The resulting beam of light

is incident on the solar cell. Two probes are placed on the cell to collect the charge carriers. For each measurement, the monochromator varies the wavelength of the incident light across a specified range in steps of 10nm. At each step, the collected current is compared to the response of a calibrated photodiode. Based on this comparison, EQE graph is developed. The software also integrates the EQE curve over the wavelength range to yield an accurate value of the J_{SC}.

An additional step is required to measure the EQE of individual subcells in a multijunction device. The current through the device at any time is limited by the subcell providing the lowest current. Thus, the measurement must be carried out such that the subcell whose EQE is being measured is the current-limiting junction. This is achieved with the use of bias lights or a bias voltage. When measuring the bottom junction in a tandem cell, an ultraviolet bias light with high photon flux can be used to saturate the top subcell. Alternatively, bias light outside the wavelength range of the top subcell can be used to saturate the bottom junction. This process becomes more complicated when the EQE graphs of the two junctions overlap significantly. In that case, bias voltages may be used as well.

3.3. Optical simulations using GENPRO4

In addition to the experiments and measurements, simulations were carried out to develop a rigorous understanding of device behaviour. Specifically, the optical behaviour of the device was simulated using GENPRO4. GENPRO4 is an optical model developed at the Delft University of Technology. It calculates the photon flux absorbed in each layer, at each wavelength, by balancing all the radiation moving towards an interface with all the radiation moving away from that interface. This is known as the net radiation method [41]. It combines ray optics and wave optics in a computationally efficient way. This model and its previous versions have been used to create demonstrably accurate simulations for a variety of solar cells [7] [12] [40] [42] [46] [55].

The inputs required to run GENPRO4 are given in the list below. The complex refractive indices are obtained from spectroscopic ellipsometry measurements. The thickness of each layer is the product of its deposition time and its deposition rate, which in turn is estimated using spectroscopic ellipsometry as well. The surface features at the interface are obtained from atomic force microscopy (AFM) measurements. The AFM measurement yields a height map of features across a small area of the surface. This height map is used in GENPRO4 to determine scattering at the interfaces.

- Wavelength dependent complex refractive index of each layer.
- Layer thicknesses.
- Features at the interfaces.
- Range of wavelengths over which the computation must be done, including step size.

In this thesis, GENPRO4 is used to simulate thin film silicon solar cells. The thicknesses of the layers are less than 1 micron, which is the coherence length of visible light. Consequently, one would expect the EQE curves of thin films cells to show interference fringes. However, no such fringes are observed. It is assumed that the scattering of light at the interfaces cancels the effects of interference. This behaviour has been approximated in the simulation by treating the intrinsic layers coherently instead. In other words, the interference effect in intrinsic layers is ignored. The doped layers and the front TCO are still treated incoherently. This approach has been successfully used in other GENPRO4 simulations of thin film solar cells as well [42].

4

Selection of a high V_{OC} top junction

4.1. Introduction

A solar-to-fuel device may be used to create syn gas from water and CO_2. In an integrated version of such a device, the high potential difference required to drive the chemical reactions is supplied by a single photovoltaic device. To this end, multijunction devices based on thin film silicon alloys may be used to generate the necessary voltage. One way to increase the V_{OC} of a multijunction device is to increase the V_{OC} of its top junction. Additionally, a number of simulation studies and theoretical analyses have shown that a wide gap ($\approx$ 2 eV) top junction can improve the overall efficiency of multijunction devices [17] [21] [54]. Intuitively, a wide gap absorber would more efficiently use high energy photons and deliver a higher V_{OC}. For these reasons, it is useful to pursue high V_{OC} cells which could be used in multijunction devices. The goal of this chapter is to suggest ways in which such a high V_{OC} cell may be achieved.

In order to achieve this goal, cells based on 2 wide bandgap absorber layers are studied: amorphous silicon (a-Si) and amorphous silicon oxide (a-SiO_X). Since the p-layers used in these cells were optimized as part of a previous MSc thesis [1], this work focuses on improving the V_{OC} by manipulating the absorber layers. Experiments were done to investigate the impact of changing various gas flows during the PECVD process. The results of these experiments are presented in the next section, which is followed by a brief conclusion in section 4.3.

4.2. Results and discussion

In a-Si cells, the absorber layer is deposited from a mixture of silane and hydrogen. In the first experiment, the effect of varying hydrogen dilution on the performance of a-Si cells was investigated. This was done by varying the silane flow while keeping the hydrogen flow constant at 200 sccm. A number of a-Si cells were deposited at different dilutions. Separately, films of a-Si were processed on flat glass at varying dilutions. This was done to better understand the changes in a-Si material with varying dilution, and how they relate to device performance. The a-Si films and absorber layers in cells were deposited at 10 mbar pressure, 9 W power, and 200 °C.

From the results in Figure 4.1, the following observation can be made. As the silane flow decreases, the bandgap widens. As a result, the V_{OC} and J_{SC} of the corresponding cell increase and decrease respectively. However, if the silane flow is decreased beyond a certain point, the trends are reversed. This transition point was found to be 1.5 sccm silane for the cells and 2 sccm for the films. This small difference may be due to minor changes in the chamber conditions, the different substrates used for cells and films, or the difference in thicknesses of the measured films. Similar trends in bandgap, V_{OC}, and J_{SC} have been reported elsewhere [6] [9] [20] [31].

These trends may be explained as follows. As the relative hydrogen flow is increased, it has been found to increase the order in the material. Several mechanisms have been proposed to explain this (selective etching [25] [50]; surface diffusion [32]; chemical annealing [29]), the details of which are

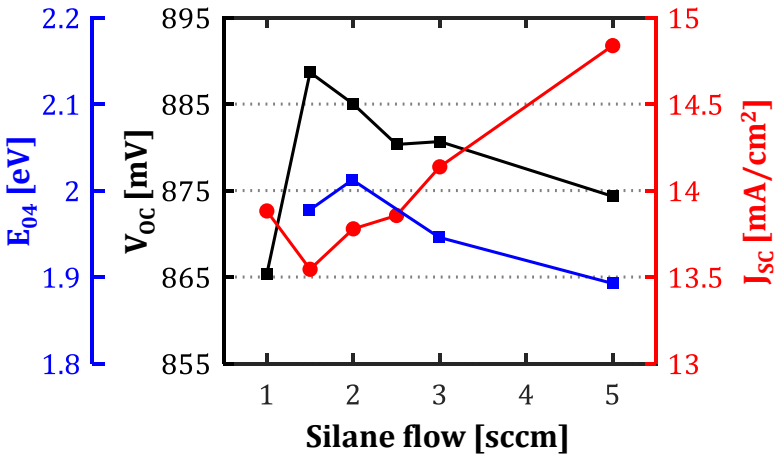

Figure 4.1: Impact of varying dilution on a-Si film bandgap and a-Si cell performance. Graph shows optical bandgap (blue) of films, V_{OC} (black) and J_{SC} (red) of the cells. The a-Si layers in all the cells were 175 nm thick. For both films and cells, a-Si was deposited at 10 mbar pressure, 9 W power, 200°C, and 200 sccm H_2.

not necessary here. Another consequence of higher dilution is a widening of the bandgap. It as been reported that, beyond a certain critical dilution, the phase of the material shifts from amorphous to nanocrystalline and this causes the drop in bandgap [9]. It is possible that this explains the trends in Figure 4.1 as well, although it is not possible to say for sure in the absence of crystallinity measurements.

a-SiO_X absorber layers are deposited by adding CO_2 to the gas mixture during PE-CVD. The effects of higher CO_2 flows with respect to silane are investigated. A number of cells, and a-SiO_X films, were deposited at different values of CO_2/SiH_4. For all these cells, the hydrogen flow and the sum of the CO_2 and SiH_4 flows was kept constant. A constant dilution was maintained to isolate the effects due to increasing relative CO_2/SiH_4. The a-SiO_X films and absorber layers were deposited at 2 mbar pressure, 3 W power, and 300 °C.

From Figure 4.2, the bandgap of a-SiO_X monotonically increases with higher CO_2 fraction. The wider bandgap causes a higher V_{OC} and a lower J_{SC}. Similar trends have been presented in other reports [13] [14] [18] [19]. In response to increasing CO_2 fraction, the fill factor first slightly increases before decreasing noticeably. The reason for the initial increase is not readily apparent. However, the deterioration of fill factor with higher CO_2 fractions may be ascribed to additional defects created by oxygen incorporation [3] [47]. The poor fill factor may also be because the rest of the device was optimized for an a-Si absorber layer, in which it case it would be possible to improve the fill factor by manipulating the doped layers.

From the above results, the highest V_{OC} obtained from a-Si and SiO_X based cells are comparable ($\approx$ 890 mV). However, a-SiO_X starts absorbing light at a lower wavelength because of its higher bandgap. There are two possible reasons why a-SiO_X based cells did not show a higher V_{OC} despite a higher bandgap. Firstly, the doped layers used in the device were optimized for the a-Si bandgap, and may be constraining the splitting of the quasi-Fermi levels in a-SiO_X. Secondly, at higher CO_2 flows, the fill factor was poor. The additional defects might increase recombination, which worsens bandgap utilization. In effect, the choice between a-Si and a-SiO_X for the top junction allows us to adjust its range of absorption without affecting the V_{OC}. This can be seen from Figure 4.3. This observation has a noteworthy consequence for multijunction design. Assuming the fill factor can be improved, a-SiO_X might be better than a-Si in structures using 3 or more junctions. The wide gap a-SiO_X would allow more light to reach the lower junctions; and reduce the spectral overlap between adjacent cells [44]. In the case of a-Si, the lower bandgap means that the desired current density can be obtained from

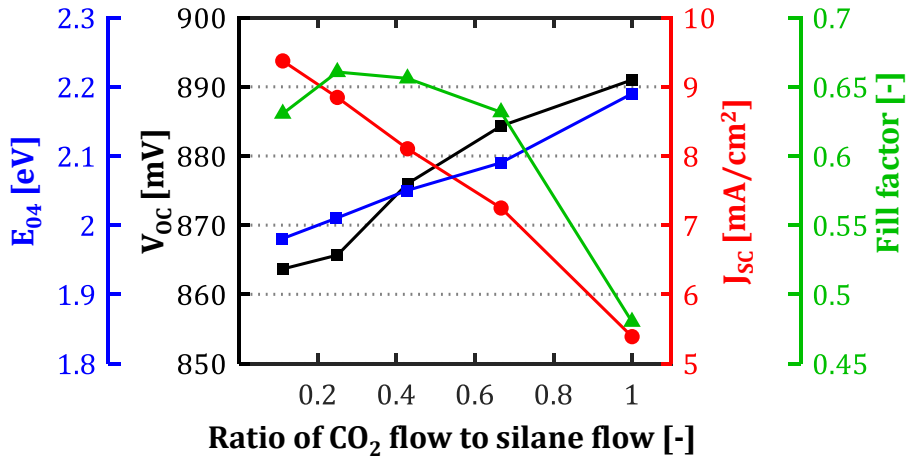

Figure 4.2: Impact of CO_2/SiH_4 on the bandgap of a-SiO_X films and performance of a-SiO_X cells. Graph shows bandgap (black) of films; V_{OC} (black), J_{SC} (red) and fill factor (green) of cells. The a-SiO_X layers in all the cells are 175 nm thick. For both films and cells, the a-SiO_X layers were deposited at 2 mbar pressure, 3 W power, 300°C, 200 sccm H_2, and 10 sccm CO_2+SiH_4.

a thinner layer. This not only reduces material consumption, but thinner layers also suffer less light-induced degradation. It should be noted that the suitability of either a-Si or a-SiO_X for the top junction will depend on the specific device structure and its intended application.

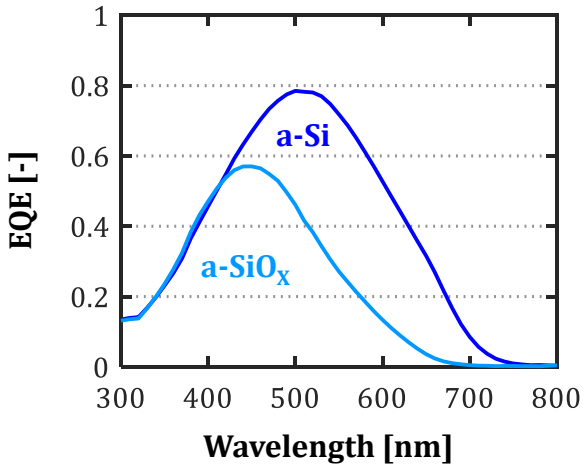

Figure 4.3: Difference in EQE of a-Si and a-SiO_X based cells. The a-Si cell shown above (dark blue) was processed at 1.5 sccm silane and had a V_{OC} of 889 mV. The a-SiO_X cell shown above (light blue) was processed at 5 sccm CO_2 and 5 sccm SiH_4. It had a V_{OC} of 891 mV.

4.3. Conclusion

The goal of this chapter was to present a high V_{OC} which may be used as the top junction in a multijunction device. To this end, cells based on a-Si and a-SiO_X were studied because of their wide bandgaps. By varying the dilution used for depositing a-Si, the V_{OC} of the a-Si cell was increased from 874 mV to 889 mV. This was the consequence of a wider bandgap. For the a-SiO_X cells, the CO_2/SiH_4 ratio was varied from 0.11 to 1. Across this range, the V_{OC} of the cell could be increased from 864 mV to 891 mV. This was also the consequence of a larger bandgap. In both cases, the highest V_{OC} obtained from our experiments were ≈ 890 mV. However, the a-SiO_X based cell was observed to start absorbing light

at an appreciably lower wavelength due to its larger bandgap. Consequently, the results presented in this chapter show that the absorption spectrum of the top junction can be varied without losing V_{OC}. This observation may be used to choose a top junction with V_{OC} and absorption properties that match the intended application.

5

Semi-empirical approach for the design of a-SiGe cells

5.1. Introduction

Amorphous silicon germanium (a-SiGe) has been used as a middle or bottom cell in tandem [5], 3-junction [4] [48] [53], and 4-junction devices [43] [45]. Depending on the device in which it is used, the optimum properties required from the a-SiGe junction can be very different. A key technique for customizing the behaviour of a-SiGe cells is bandgap profiling. This refers to the variation of the bandgap along the width of the absorber layer. The bandgap may be profiled in a number of ways; and experimentally investigating the optimum bandgap profile for a particular application can be cumbersome. Therefore, this chapter seeks to lay down a novel, semi-empirical method for finding the optimum bandgap profile.

Before discussing the results, the method used to profile the bandgap for this study is discussed in some detail. The bandgap was profiled by varying the germane (GeH_4) flow during PECVD. This is because the germane was found to linearly change the bandgap for the deposition conditions used, as shown in Figure 5.1. However, the bandgap is not the only parameter that changes with varying GeH_4 flow. A-SiGe with higher concentrations of Ge will have different structural properties, and its growth or deposition rate can be expected to be different. Thus, the deposition rate of a-SiGe must be estimated as a function of the GeH_4 flow rate.

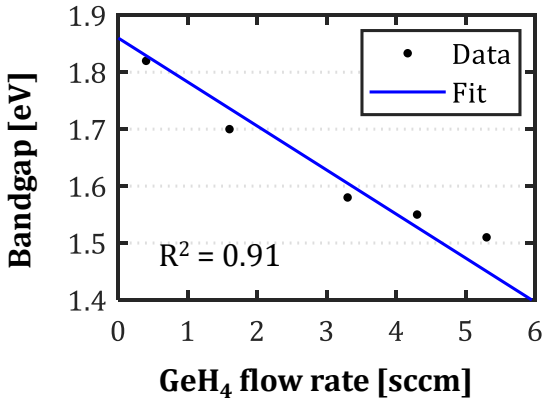

Figure 5.1: Variation of optical bandgap with germane flow. Black dots indicate values of optical bandgap measured from a-SiGe films deposited at different germane flows. The blue line is a linear equation fitted to the data.

To do this, a set of a-SiGe films was deposited on flat glass at different germane flow rates. The flow rate was varied in discrete steps of ≈ 1 sccm. The deposition rate for different germane flows was determined by dividing the thickness of the film (measured using ellipsometry) by its deposition time. The deposition rate was then assumed to vary linearly with germane flow from one measured value to the next. This variation of deposition rate with GeH_4 flow is shown in Figure 5.2.

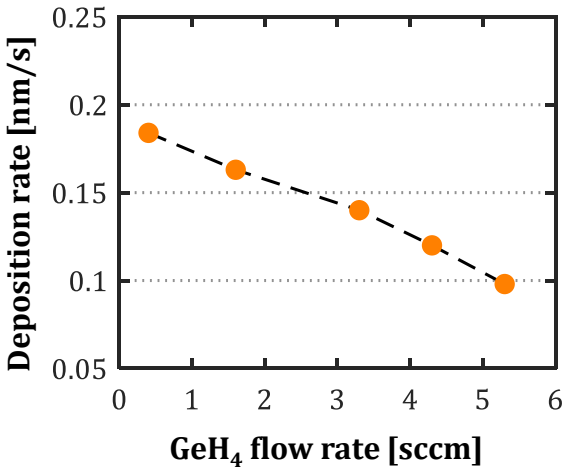

Figure 5.2: Variation of a-SiGe deposition rate with changing GeH_4 flow. The orange circles indicate measurements of deposition rates from a-SiGe films deposited at different GeH_4 flows. The dashed black lines indicate the regions over which the deposition rate is assumed to be varying linearly with GeH_4 flow.

For illustrative purposes, we consider the deposition of a 100 nm thick a-SiGe layer. Based on the equation visualized in Figure 5.1, the GeH_4 flow rate needs to linearly ramp up from 0 to 4.3 sccm across this 100 nm region. To implement this in the PECVD equipment, the 100 nm layer is divided into (say) 20 sub-layers, each 5 nm thick. The GeH_4 flow is then ramped up to the desired value in 20 steps. Each 5 nm sub-layer is deposited at a slightly different GeH_4 flow. The thickness of each sub-layer is controlled using the deposition rates shown in Figure 5.2. The germane flow profile during the first five minutes of deposition of this 100 nm layer is shown in Figure 5.3. Although the machine is instructed to change the GeH_4 flow instantaneously, it takes some time (≈ 10-15 seconds) for the chamber plasma to reflect the new flow rate. This ”retention time” results in a smoother profiling of the bandgap. This is how the a-SiGe bandgap was profiled for this study.

A generalized depiction of a profiled bandgap, along with the corresponding germane flow, is given in Figure 5.4. In Figure 5.4, the width of the i-p region (distance between i-p interface and the closest point of minimum bandgap) is given by w_1. The width of the plateau region (region of minimum bandgap, deposited at the maximum germane flow f_{peak}) is $w_2 - w_1$. For convenience, this is written as $W\Delta w$, where W is the total width of the absorber and Δw is the plateau fraction. Another feature of the bandgap profile is the minimum bandgap, which can be estimated from the equation visualized in Figure 5.1 and the peak germane flow. In the experiments done for this study, the ratio of the i-p width (w_1) to the i-n width ($W - w_2$) was kept constant. Consequently, the bandgap profile could be decomposed into a set of 3 features or variables: W, Δw, and f_{peak}. The rest of this chapter is devoted to analysing how these 3 features affect device performance.

Experiments were done to investigate the impact of each of the aforementioned variables on the J_{SC} and V_{OC} of a-SiGe cells. The results of these experiments are discussed in section 5.2. An accurate idea of the thicknesses of the a-SiGe layers is necessary to properly interpret the experimental data. At the same time, reliably determining the thicknesses of profiled a-SiGe layers is fraught with challenges. Firstly, thickness measurements are done on flat glass whereas the layers in the actual cell are processed on textured glass. Secondly, the a-SiGe layers in cells are grown on top of n-doped substrates. Thirdly, there may be experimental errors in the measurements used to determine the

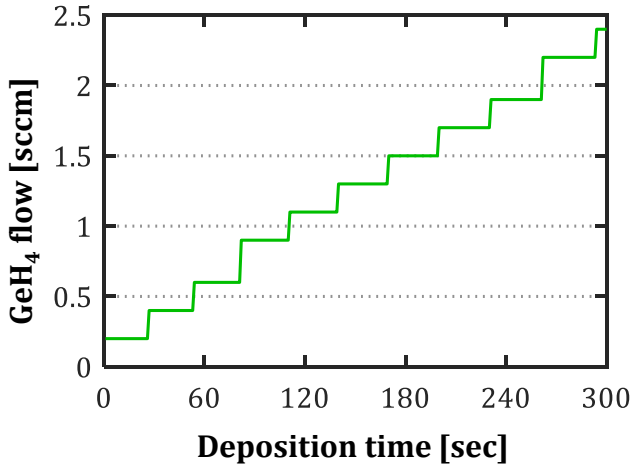

Figure 5.3: The germane flow profile for the first five minutes of deposition of a 100 nm a-SiGe layer with a bandgap profile.

deposition rates (refer Figure 5.2). Fourth, the smoothing of the GeH_4 flow profile due to a non-zero retention time may affect the thickness of the deposited sub-layers. Finally, the a-SiGe deposition in cells is followed by the deposition of p-doped layers using a H_2-rich plasma which could potentially etch away some of the a-SiGe material. Thus, there is good reason to doubt the experimentally estimated thicknesses. In order to obtain more a more accurate idea of the thicknesses, optical simulations of the cells were done using GENPRO4. A distinction is therefore made between the ”estimated thickness” expected from measurements and the ”simulated thickness” obtained from GENPRO4. The details of these simulations are presented in section 5.3.

Thus, using experiments and optical simulations, it was possible to get an accurate idea of how $W, \Delta w$ and f_{peak} individually affect cell performance. To investigate the impact of varying all these features simultaneously, a set of semi-empirical relations was developed. They are ”semi-empirical” because they are motivated from theoretical considerations and then fitted to experimental data. For both J_{SC} and V_{OC}, the effect of changing all 3 features of the bandgap profile could be (approximately) expressed in a single equation. This is a key contribution of this chapter. The semi-empirical approach to approximately analyse how device performance changes with bandgap profiling is relatively novel and may be used to expedite the design of a-SiGe cells for a variety of applications. The equations used, and the resulting insights into cell design, are discussed in section 5.4.

5.2. Experimental results

This section discusses the results of experiments performed to investigate the impact of varying individual features of the bandgap profile on the cell performance.

5.2.1. Thickness series

The thickness of the a-SiGe layer was varied while the peak germane flow rate was held constant at 4.3 sccm. The bandgap of these absorbers had 0% plateau (i.e., a V-shaped profile). The ratio of the i-p width to the i-n width was held constant. Thus, increasing the total thickness has the effect of proportionately increasing the i-p and i-n region widths. From the results in Figure 5.5, it can be seen that the J_{SC} of the cell increases monotonically with the thickness of the absorber. This is because photons with lower energies have a lower probability of absorption, and are more likely to be absorbed if they travel longer distances inside the absorber. This can be seen in Figure 5.6 as well - thicker absorbers show an improved EQE for relatively low-energy photons (600-800 nm).

Increasing the thickness also results in a lower V_{OC} (Figure 5.5). As mentioned earlier, by increasing the thickness we are simultaneously varying the i-p and i-n region widths. Both of these parameters affect the cell V_{OC} in complicated ways. For the trend observed in Figure 5.5, the decrease in V_{OC} is

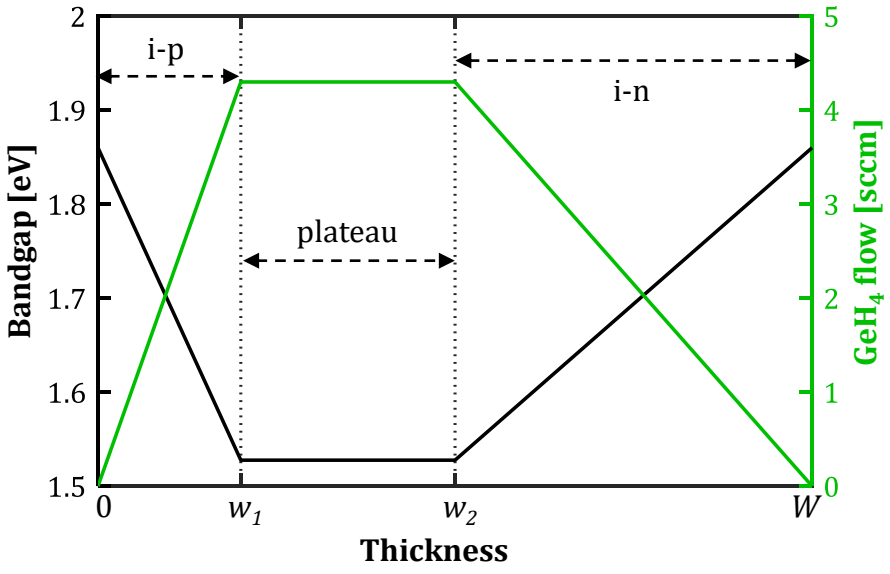

Figure 5.4: A generalized depiction of a profiled bandgap across the thickness of the absorber. The green line shows the germane flow used to deposit the a-SiGe material of a certain bandgap. The i-p region refers to the distance between the i-p interface and the point of minimum bandgap. The plateau region refers to the material deposited at the minimum bandgap. The space between the end of the plateau and the i-n interface is called the i-n region. The width of the i-p region is denoted by w_1, the width of the plateau region is denoted by $w_2 - w_1$, and the total width of the absorber layer is W.

presented as the net result of two competing processes. Firstly, increasing the thickness is expected to lead to an increase in bulk recombination. This is because the charge carriers need to travel through a longer distance inside the defect-rich a-SiGe material before being collected. The increased bulk recombination current leads to a lower V_{OC} [34]. On the other hand, the thicker absorbers in our experiments also have higher i-p region widths. It has been reported that the V_{OC} should, in fact, increase as the point of minimum bandgap is moved further away from the i-p interface [8] [57]. From the experimental results, it may be argued that the V_{OC}-decreasing effects of bulk recombination outweigh the V_{OC}-boosting effects of a larger i-p region in the observed range. Overall, the decrease in V_{OC} is small (< 20 mV) relative to the gain in J_{SC} ($\approx$ 1.5 mA/cm^2) as the thickness is increased from 160 nm to 230 nm.

5.2.2. Plateau series

The plateau fraction of the bandgap profile was increased from 0% to 50% of a 160 nm thick absorber deposited with a peak germane flow of 4.3 sccm. As was the case for the thickness series, the ratio of the i-p and i-n widths was kept constant. As the plateau fraction was increased, the i-p and i-n region widths were decreased. Increasing the plateau leads to an increase in J_{SC}, as shown in Figure 5.7. From the EQE plots shown in Figure 5.8, the increase in current density comes primarily from photons in the 600-800 nm wavelength range. In this respect, the effect of increasing plateau fraction is similar to the effect of increasing thickness. This may be explained as follows. As the plateau fraction increases, the average bandgap of the absorber decreases. This increases the probability of absorption of all photons with energies above the bandgap. Most of the highly energetic photons (300-400 nm) are absorbed in the first few nanometres of the absorber. Thus the effect of increasing plateau is more pronounced at higher wavelengths.

Increasing the plateau fraction also leads to a decrease in the V_{OC}, as shown in Figure 5.7. This may be due to a couple of reasons. Firstly, the average bandgap of the a-SiGe layer is reduced. Secondly, there is less distance between a-SiGe have the minimum bandgap and the dominant i/p junction [8]. Thirdly, the larger fraction of a-SiGe deposited at a high GeH_4 flow may be more defective,

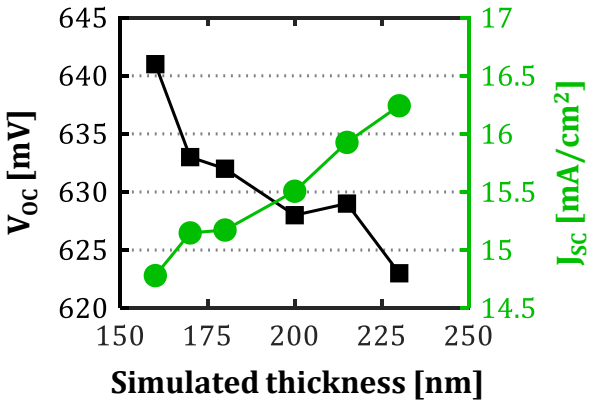

Figure 5.5: Effect of thickness on device performance. The thicknesses given along the x-axis were obtained from GENPRO4 simulations. a-SiGe was deposited with a V-shaped profile, a peak GeH_4 flow of 4.3 sccm, SiH_4 flow of 30 sccm, H_2 flow of 200 sccm, 3.6 mbar pressure, and 3 W power.

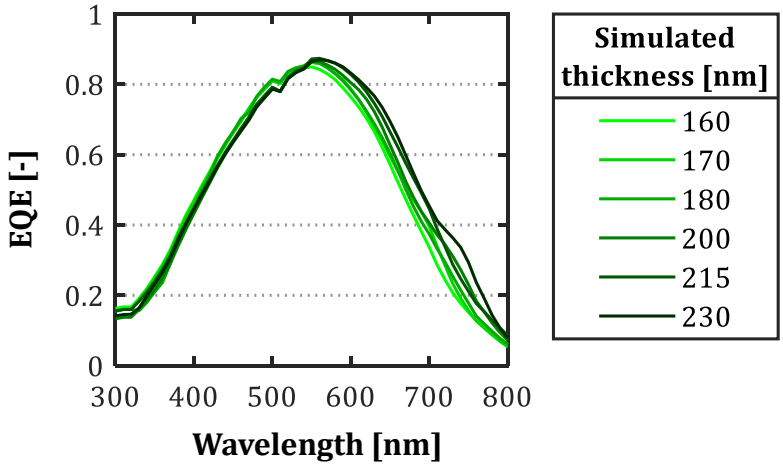

Figure 5.6: Effect of thickness on EQE. a-SiGe was deposited with a V-shaped profile, a peak GeH_4 flow of 4.3 sccm, SiH_4 flow of 30 sccm, H_2 flow of 200 sccm, 3.6 mbar pressure, and 3 W power.

which increases bulk recombination.

5.2.3. Peak germane flow series

The peak germane flow used during deposition was varied between 1.6 sccm and 4.3 sccm in a 160 nm absorber with a V-shaped bandgap profile. As the peak flow is increased, the i-p and i-n widths remain constant but the bandgap gradient across each of these regions increases. From Figure 5.9, the V_{OC} decreases monotonically with increasing germane flow. This may be because a decrease in the minimum bandgap constrains the extent to which the quasi Fermi levels in the absorber can split. Additionally, higher GeH_4 flows make the material more defective, increasing recombination. The reduced bandgap of the material at higher peak flows also explains the increase in J_{SC} (Figure 5.9). Higher peak flows have the effect of changing the wavelength at which absorption starts, as shown in Figure 5.10.

5.3. GENPRO4 simulations

As discussed in the introduction, there are some inherent challenges in determining the thicknesses of the profiled a-SiGe absorbers as used in this study. Thus, optical simulations were done on GENPRO4

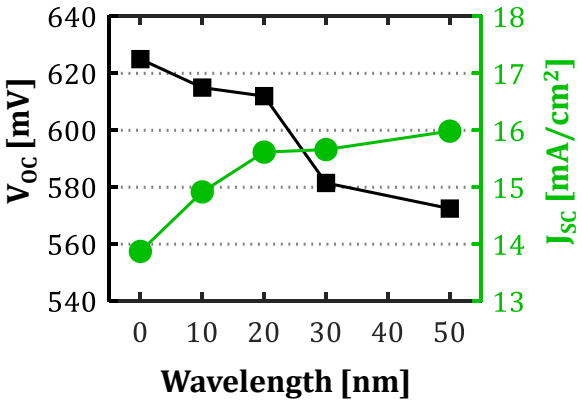

Figure 5.7: Effect of plateau fraction on device performance. 160 nm thick a-SiGe was deposited with a peak GeH_4 flow of 4.3 sccm, SiH_4 flow of 30 sccm, H_2 flow of 200 sccm, 3.6 mbar pressure, and 3 W power.

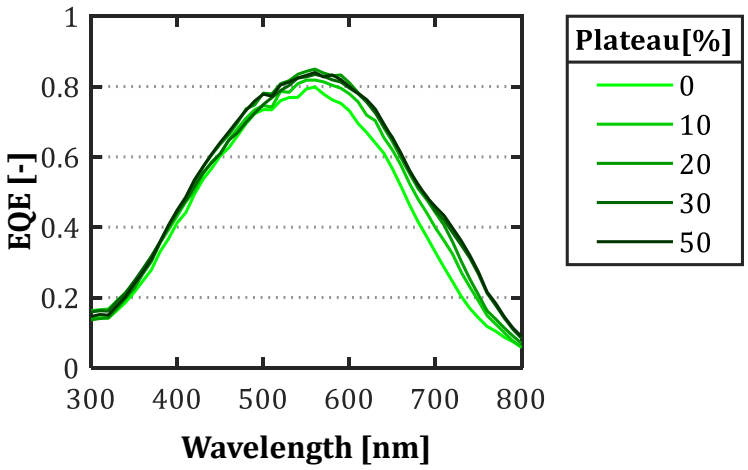

Figure 5.8: Effect of plateau fraction on EQE. 160 nm thick a-SiGe was deposited with a peak GeH_4 flow of 4.3 sccm, SiH_4 flow of 30 sccm, H_2 flow of 200 sccm, 3.6 mbar pressure, and 3 W power.

to obtain a reliable estimate of the actual thicknesses.

Due to differences in PECVD conditions and the conditions under which ellipsometry measurements are performed, the optical properties of the layers in the cell may diverge from what is measured. To account for this deviation and accurately simulate the devices, a wide variety of thin films were processed and measured. These include doped layers processed with varying dopant flows, oxygen fractions, and deposition powers as well as undoped a-SiGe films at different germane flow rates. In addition, the surface roughness of the textured glass was measured using atomic force microscopy to simulate the texture at the layer interfaces.

With the help of this diverse set of data on refractive indices and surface texture, realistic optical models were developed. The simulation parameters (layers, thicknesses, and order of stacking) were systematically varied until the simulated absorbance of the absorber layer closely matched the measured EQE for all the cells. In the final GENPRO4 model, it was possible to replicate the EQE curves of all 3 experimental series by only manipulating the relevant variable (i.e., thickness, plateau fraction, or peak flow rate). The final simulation parameters are given in Table 5.1 alongside the deposition parameters. The simulated absorptance and measured EQE of the first point of the thickness series is shown in Figure 5.11. Similar graphs for the entire thickness series, plateau series, and peak flow series are given in Appendix A. The successful reproduction of the experimental data by varying just a single model parameter suggests that the simulations closely mirror the actual device. It is therefore

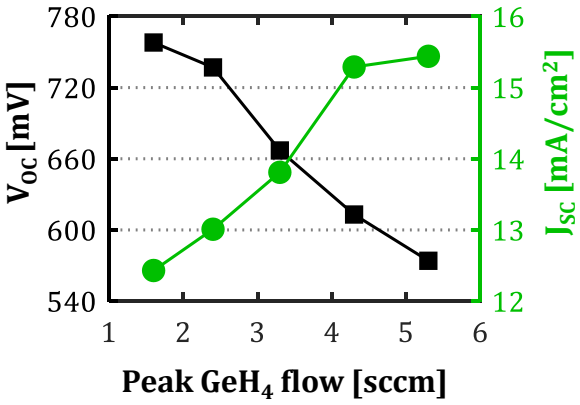

Figure 5.9: Effect of peak GeH_4 flow on device performance. 160 nm thick a-SiGe was deposited with a V-shaped profile, SiH_4 flow of 30 sccm, H_2 flow of 200 sccm, 3.6 mbar pressure, and 3 W power.

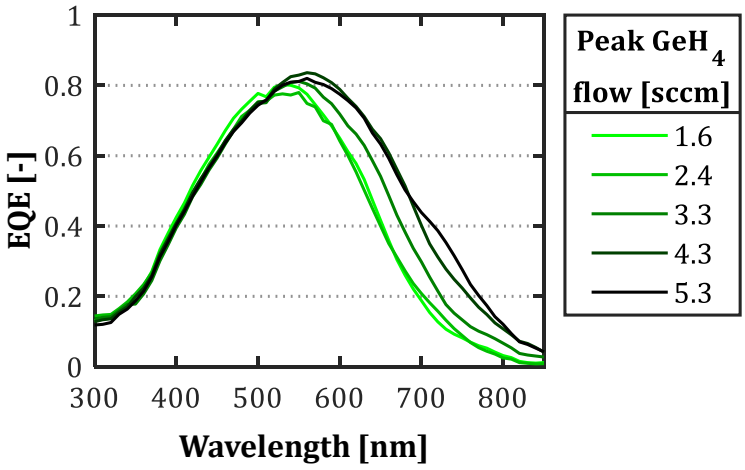

Figure 5.10: Effect of peak GeH_4 flow on EQE. 160 nm thick a-SiGe was deposited with a V-shaped profile, SiH_4 flow of 30 sccm, H_2 flow of 200 sccm, 3.6 mbar pressure, and 3 W power.

inferred that the thicknesses used in these simulations are a reasonably accurate representation of reality.

5.4. Relation between bandgap profile and device performance

Using a combination of experimental data and optical simulations, it was possible to obtain reliable data on how individual features of the bandgap profile affect device performance. In this section, we present a set of semi-empirical relations which show how all 3 variables (thickness, plateau, and peak flow) collectively govern the cell J_{SC} and V_{OC}.

The goal here is not to present mathematically exact equations which express detailed physical truths. Instead, the emphasis is on laying down an expedient, semi-empirical approach to optimum bandgap profiling in a-SiGe cells. As such, several simplifying assumptions were made to obtain the equations. The impact of different doped layers, various interface effects, and the continuous nature of the distribution of Ge in the absorber were not taken into account. Furthermore, the values of the constants in the equations were obtained by fitting the equations to the experimental data shown in section 5.2. Fitting the same set of equations to different experiments would yield other constants. As such, the absolute values of the J_{SC} and V_{OC} are not as important as the trends in these values in response to changes in bandgap profile. Thus, with the help of simplifying assumptions, we are able to present a useful approach for investigating the impact of bandgap profiling on cell performance in

Deposited Layer	Estimated thickness	Simulated Layer	Simulated thickness
p-nc-Si	3nm	p-nc-Si	3nm
p-SiO_X at 1.8sccm CO_2	16nm	p-SiO_X at 3.2sccm CO_2 p-SiO_X at 1.6sccm CO_2	3nm 15nm
i-nc-Si	6nm	i-nc-Si	3nm
a-SiGe (variable GeH_4 flow)	(variable; with a fixed i-p to i-n width ratio)	a-SiGe at 1.6sccm GeH_4 a-SiGe at 3.3sccm GeH_4 a-SiGe at 4.3sccm GeH_4 a-SiGe at 3.3sccm GeH_4 a-SiGe at 1.6sccm GeH_4	(variable; with a fixed i-p to i-n width ratio)
n-a-Si	4nm	n-a-Si	4nm
n-SiO_X at 1.6sccm CO_2	8.5nm	n-SiO_X at 1.6sccm CO_2	8.5nm
n-SiO_X at 0.8sccm CO_2	8.5nm	n-SiO_X at 0.8sccm CO_2	8.5nm
n-nc-Si	9nm	n-nc-Si	9nm

Table 5.1: Comparison of the simulated and deposited layers. The above parameters remain the same for all the GENPRO4 simulations done in this study.

an approximate way.

We first consider the J_{SC}. As observed in section 5.2, the peak germane flow affects the wavelength at which absorption starts by changing the minimum bandgap inside the a-SiGe layer. In other words, the peak flow caps the maximum value of the J_{SC}. From Lambert-Beer's Law, we know that the intensity of light decays exponentially inside an absorptive medium. Thus, intuitively, the J_{SC} may be expressed as follows:

$$J_{SC} = \text{Peak flow factor } x \text{ Exponential decay factor}$$

The extent of the exponential decay is higher in thicker layers and in layers with higher absorption coefficients. In other words, the exponential decay term depends on the thickness and the plateau fraction of the absorber layer.

$$J_{SC} = \text{Peak flow factor } x \text{ Exponential decay } (W, \Delta w)$$

The complete equation can be written as:

$$J_{SC} \approx A\{1 - exp(-BW - CW\Delta w)\} \tag{5.1}$$

where

$$A \approx \frac{K_1}{(E_{04})^2} + \frac{K_2}{E_{04}} + K_3 \tag{5.2}$$

and

$$E_{04} \approx 1.86 - 0.073 f_{peak} \tag{5.3}$$

In the equations above, A, B, C, K_1, K_2, and K_3 are constants. The values of these constants obtained after fitting the above equations to the experimental data are given in Table 5.2. The step-by-step derivation for the equations in given in Appendix B.

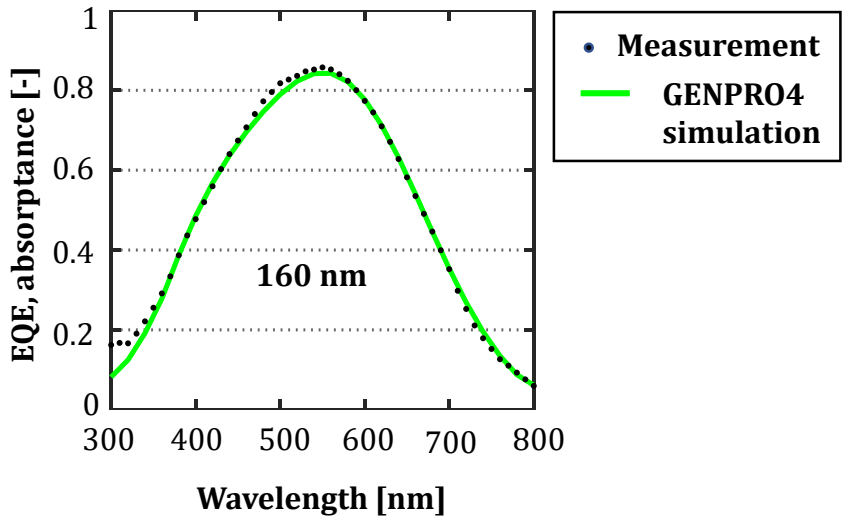

Figure 5.11: Comparison of the measured EQE and simulated absorptance for an a-SiGe cells with a 160 nm absorber with a V-shaped profile and peak germane flow of 4.3 sccm.

Constant	Value
K_1	-149.1
K_2	222.7
K_3	-64.35
B	0.0119
C	0.01226

Table 5.2: Values of constants in equations 5.1 and 5.2. These values were obtained by fitting the equations to the measured data.

Equations 5.1, 5.2, and 5.3 collectively describe how all 3 variables (thickness, plateau, and peak flow) affect the J_{SC}. Contour plots based on these equations are given in Figure 5.12. The contour lines in Figure 5.12 show how different combinations of thickness, plateau fraction, and peak germane flow can yield the same J_{SC}. In the given ranges for these variables, it appears that plateau fraction and thickness are somewhat equally interchangeable. Peak germane flow, on the other hand, is a much stronger determinant of J_{SC} than the other parameters. However, based on the EQE data, we know that the three variables increase absorption in different ways. The germane flow changes the wavelength at which absorption starts. Thicker layers and/or layers with larger plateaus absorb more photons close to the bandgap (Figures 5.6 and 5.8). Keeping this in mind, the semi-empirical approach laid out here has 2 distinct advantages. It firstly allows us to vary the J_{SC} from the device by bandgap profiling. More interestingly, it also gives us some control of the wavelength range over which the absorption occurs (keeping J_{SC} constant). These advantages are particularly important in the context of multijunction cell design. The given approach can help us to improve current-matching in multijunction devices and reduce spectral overlap between adjacent junctions.

Equations 5.1 - 5.3 ignore several subtleties of cell behaviour. The absorption coefficient (which affects the rate of exponential decay) of a profiled a-SiGe is expected to vary continuously across its width, but the given equations assume a fixed value of the absorption coefficient for each of the 3 regions (i-p, plateau, i-n). The i-p region width affects the amount of absorption. The equations, on the other hand, assume that the J_{SC} only depends on thickness and plateau fraction, not the location of the plateau. These factors were simplified out of our equations because the emphasis was on developing a convenient approach to a-SiGe cell design based on approximate relationships.

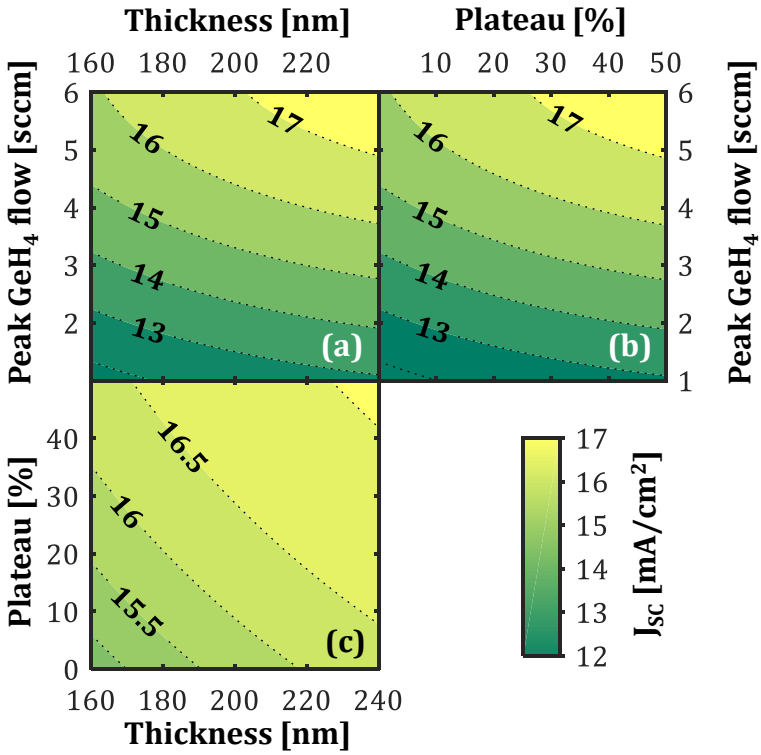

Figure 5.12: Effect of varying different features of the bandgap profile (thickness, plateau fraction, peak flow) on the J_{SC} of a-SiGe devices. The plots shown above were obtained by fitting the equations 5.1 and 5.2 to the measured data.

We now consider the V_{OC}. It is quite challenging to analyse the V_{OC} because it depends on a variety of material factors in complicated ways. Nonetheless, the following equation has been found to hold for the V_{OC}

$$V_{OC} \approx \frac{nk_BT}{q} ln\left(\frac{J_{SC}}{J_0}\right) = \frac{nk_BT}{q}\{ln(J_{SC}) - ln(J_0)\} \tag{5.4}$$

where n is the ideality factor, k_B is the Boltzmann constant, and T is the absolute temperature. J_0 is the saturation current density, which is a measure of the amount of recombination in the device. As thickness increases, bulk recombination in the device may increase. This was experimentally observed, as shown in Figure 5.5. Furthermore, higher Ge-incorporation can lead to more defect sites, which can increase recombination. Thus, the J_0 depends on all 3 features of the bandgap profile (thickness, plateau, and peak flow). Thus, generally

$$V_{OC} \propto \ln(J_{SC}) \text{ - Recombination}(W, \Delta w, f_{peak})$$

where the J_{SC} itself is a function of the bandgap profile as given in Equation 5.1. The complete equation may be written as:

$$V_{OC} \approx D ln\left(\frac{J_{SC}}{W}\right) - E f_{peak}(1 + \Delta w) + F \tag{5.5}$$

The values of the constants $D, E,$ and F are given in Table 5.3. The detailed derivation for the above relation is given in Appendix B.

Contour plots based on equation 5.5 are shown in Figure 5.13. From Figure 5.13, it appears that the thickness of the absorber affects the V_{OC} much less than the peak flow or plateau in the observed

Constant	Value
D	52
E	35
F	910

Table 5.3: Values of constants used in equations 5.4 and 5.5. These values were obtained after fitting the equations to the experimental data.

range. At this point, it is important to note that this model ignores some of the nuances of cell behaviour. The most important of these relate to the nature of recombination, which can be quite challenging to model. Firstly, the peak germane flow and plateau region also affect the amount of recombination in the device by changing the defect density, but the model assumes recombination to be solely a function of thickness. Secondly, all changes in V_{OC} have been assumed to depend on bulk changes, which ignores mechanisms such as recombination at the i-p interface. Thirdly, it has been shown that the narrowing of the bandgap due to Ge-incorporation may not be symmetrically divided between the conduction and valence band edges [57]. Depending on which band edge is distorted to what extent, the extent to which the quasi-Fermi levels can split may vary. These mechanisms were simplified out of our model for the sake for expediency, and the graphs presented in Figure 5.13 should be viewed in this context. Nonetheless, our semi-empirical approach is able to suggest a range over which the a-SiGe V_{OC} may be varied with bandgap profiling. Furthermore, Figure 5.13 (b) also proposes different combinations of plateau and peak flow which may be used to extract a given V_{OC}.

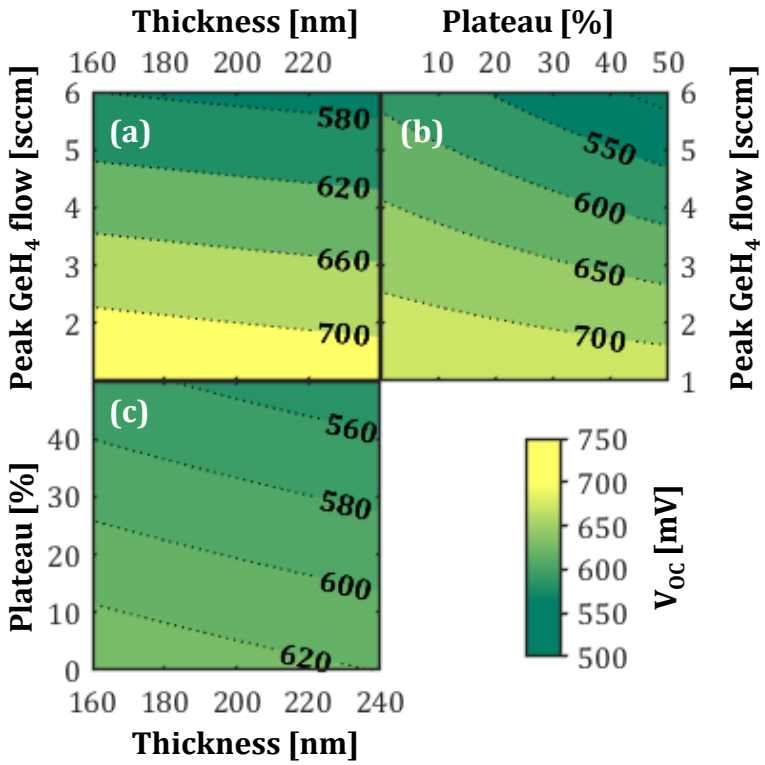

Figure 5.13: Effect of varying different features of the bandgap profile (thickness, plateau fraction, peak flow) on the V_{OC} of a-SiGe devices. The plots shown above were obtained by fitting the equations 5.4 and 5.5 to the measured data.

5.5. Conclusion

In this chapter, a semi-empirical approach for optimally designing a-SiGe cells was presented. First, experiments were done to investigate how different features of the a-SiGe bandgap profile affect cell performance. Secondly, optical simulations on GENPRO4 were performed to obtain a more accurate estimate of the thickness of the deposited a-SiGe layers. Thirdly, a set of semi-empirical relations between cell performance (J_{SC}, V_{OC}) and bandgap profile were fitted to the experimental data. These relations were finally used to visualise how the J_{SC} and V_{OC} might evolve as the different features of the bandgap profile are varied simultaneously. The models used are only approximate and don't account for several nuances of device performance. Nonetheless, they represent an expedient approach for optimally profiling a-SiGe cells.

6

Systematic optimization of tunnel recombination junctions

6.1. Introduction

Tunnel recombination junctions (TRJ) affect device performance in a number of ways. The doped layers need to generate a strong enough electric field across their respective subcells to have good carrier collection. At the same time, the n/p junction itself should remain Ohmic and not generate a reverse bias voltage under illumination. The transverse conductivity of the doped layers affects the transport of carriers across the doped layers towards the n/p interface, where the amount of recombination is determined by several material properties such as defect density and activation energy. In addition to these electrical effects, the TRJ has an optical role to play as well. The reflective properties of the TRJ affect how much light is reflected back up into the top junction, which affects current matching. Additionally, the layers in the TRJ themselves should have a wide bandgap in order to minimize parasitic absorption. These are some of the ways that the TRJ influences device performance. By substituting one layer in the TRJ for another, often more than one of the above mechanisms is affected. This makes it difficult to pinpoint the origin of observed changes in performance as a result of variations in processing conditions. This problem is compounded by the fact that there is some difference in the quality of the processed layer that occurs randomly from one deposition to the next.

The fact that more than one property of the TRJ changes at once also makes it difficult to explain the observed trends in the data with confidence. Furthermore, the explanation of trends is quite challenging because the growth of the thin films in question is quite complex, especially at very small thicknesses (few tens of nanometres). Consequently, the material properties of the films are difficult to ascertain, even though they affect important properties of the TRJ such as defect density and transverse conductivity. Thus, the optimization of tunnel recombination junctions is a challenging task because of the complexities of the TRJ itself and the difficulties associated with processing.

In light of the above, a systematic approach was adopted. The TRJ was disaggregated into the p-doped part and the n-doped part. Each of these was studied separately. First, different combinations of p-type materials were tried at the TRJ. After identifying the best performing p-layer, its thickness was varied. This was followed by a similar optimization method used for the n-doped parts. A large number of cells were processed in order to systematically investigate the effects of different variables. Unfortunately, some of the cells encountered processing errors and could not be used for analysis. The complete set of measurements are presented in Appendix D. Even so, the remaining, usable data allowed us to present some insights into the performance of different TRJs. These results are discussed in the following sections.

6.2. Optimization of p-doped layers

The different p-layers tested are shown in Table D.1. The exact deposition conditions of each layer are given in the Appendix C. From P1 to P3, the diborane flow in the plasma chamber is increased for the p-

layer at the n/p interface. This allows us to investigate the effect of increasing the dopant concentration at the n/p interface. For P4 and P5, a thin layer of p-nc-Si is used at the n/p interface instead of p-nc-SiOx. By comparing P4 and P5 with layers P1-P3, we can see the effect of a silicon oxide phase at the n/p interface. The p-nc-Si layer in P4 is deposited at a higher ratio of diborane flow to silane flow, higher dilution, and lower power. In effect, these changes were expected to reduce the activation energy in P4 with respect to P5. The higher dilution improves the crystallinity of the layer [56]. The higher crystallinity may contribute to increased doping. In a-Si alloys, boron might be incorporated into a 3-fold or 4-fold coordinated site, and the former are non-doping [51]. Improved crystallinity reduces the concentration of the 3-fold coordinated sites, and in this way contribute to a larger fraction of active dopants. The increased density of holes in P4 consequently pull the Fermi level closer to the valence band edge, reducing the activation energy. In sum, the different p-layers were chosen in a such a way that the effects of oxygen content, doping, and activation energy could be investigated.

Ideally, the results of the experiments with both sets of tandems would be studied together. The identification of common trends could have helped identify better performing p-layers with greater certainty. Unfortunately, the a-Si/a-SiGe cells deposited with the layers P1-P3 encountered problems during deposition. These problems affected the series and shunt resistances of these cells, effectively masking any trends due to differences in the TRJ. Thus, all 5 TRJs are compared for the a-SiGe/nc-Si tandem and the layers P4 and P5 are additionally compared for the a-Si/a-SiGe tandem.

Name	Composition
P1	12 nm p-nc-SiO_X
P2	6nm p-nc-SiO_X+ 6nm p-nc-SiO_X
P3	6nm p-nc-SiO_X++ 6nm p-nc-SiO_X
P4	3 nm p-nc-Si_{low} 9nm p-nc-SiO_X
P5	3 nm p-nc-$Si_{35\ W}$ 9nm p-nc-SiO_X

Table 6.1: Different combinations of p-type materials investigated for use in tunnel recombination junctions.

The performance of a-SiGe/nc-Si tandems deposited with the 5 different TRJs are shown in Table D.8. Moving from P1 to P3, the fill factor is observed to improve. This increase in fill factor is despite the fact that current matching is improved. This is interesting because a correlation between current mismatch and fill factors has been reported [52]. This trend is also observed in moving from P4 to P5. An increase in doping might affect the fill factor in a number of ways. Firstly, a more heavily doped p-layer would generate a stronger electric field across the nc-Si absorber. This would enhance the collection of holes at the i/p interface of the nc-Si subcell. Secondly, increasing the boron flow suppresses crystalline growth, which in turn has 2 effects [28]. On one hand, the more amorphous material has a lower conductivity. On the other hand, it also has a greater fraction of dangling bonds which serve as recombination centers. Thus, increasing the doping may improve hole collection and recombination but adversely affect conductivity. For the chosen deposition conditions, and the range over which doping is increased, the net result of the aforementioned competing processes appears to be an increase in fill factor with doping.

Additionally, the cells deposited with P1-P3 have higher fill factors than those deposited with P4 and P5. This may suggest that it is beneficial to have an amorphous SiO_X phase at the n/p interface. The presence of an amorphous SiO_X phase at the n/p interface appears to improve fill factor. The higher oxygen content suppresses crystalline growth [24], which increases the density of defect states. This may contribute to improved recombination of charge carriers when compared to a TRJ with a p-nc-Si layer at the p/n interface. Alternatively, the better performance of cells using P1-P3 may be because

of a difference in the thickness of the p-layer at the n/p interface. P4 and P5 use a 3 nm p-nc-Si layer. In the deposition of nanocrystalline silicon, there is an initial, incubation period of amorphous growth [11]. Thus, it is possible that the 3 nm p-nc-Si layer does not possess sufficient crystallinity. This may reduce the efficiency of boron doping, and consequently increase the activation energy.

The layers P4 and P5 were additionally deposited in a-Si/a-SiGe tandems. The cell deposited with P4 was found to have a higher fill factor and V_{OC}. Observing the results in Table D.8, the a-SiGe/nc-Si tandem deposited with P4 had a higher V_{OC} but a lower fill factor. This indicates that the lower activation energy of the p-nc-Si layer indeed is beneficial for the V_{OC}. With respect to the fill factor, it is not clear why there is a difference in trends for a-Si/a-SiGe and a-SiGe/nc-Si. On one hand, random variations in processing may be masking the beneficial effect of the low activation energy in P4. On the other hand, it is also possible that the difference is due to the different behaviour of the subcells in the two tandems.

	Units	**P1**	**P2**	**P3**	**P4**	**P5**
V_{OC}	mV	1113	1114	1112	1120	1110
J_{SC} a-SiGe	mA/cm^2	15.69	15.36	15.17	15.17	14.74
J_{SC} nc-Si	mA/cm^2	5.47	5.60	5.68	5.45	6.11
Fill factor	-	0.707	0.717	0.725	0.668	0.687
Efficiency	%	4.30	4.47	4.58	4.08	4.66

Table 6.2: Effect of varying the combination of p-layers at the TRJ in a-SiGe/nc-Si tandems.

From the available results, P3 was chosen as the best performing TRJ for the a-SiGe/nc-Si tandem and P4 was chosen for the a-Si/a-SiGe tandem. Two series of tandems were processed where the thickness of the best-performing p-layer in the TRJ was varied. The total thickness was varied from 5 nm to 25 nm for both P3 and P4. The thicknesses of the individual p-layers in P3 and P4 are given in Table 6.3. Unfortunately, the a-Si/a-SiGe tandems deposited with 20 nm and 25 nm thick p-layer had processing problems. Their results could not be used for analysis.

Total thickness	**Thickness of layers in P3**	**Thickness of layers in P4**
5 nm	2.5 nm p-nc-SiO_X++ 2.5 nm p-nc-SiO_X	2 nm p-nc-Si 3 nm p-nc-SiO_X
10 nm	5 nm p-nc-SiO_X++ 5 nm p-nc-SiO_X	3 nm p-nc-Si 7 nm p-nc-SiO_X
15 nm	6 nm p-nc-SiO_X++ 9 nm p-nc-SiO_X	3 nm p-nc-Si 12 nm p-nc-SiO_X
20 nm	6 nm p-nc-SiO_X++ 14 nm p-nc-SiO_X	3 nm p-nc-Si 17 nm p-nc-SiO_X
25 nm	6 nm p-nc-SiO_X++ 19 nm p-nc-SiO_X	3 nm p-nc-Si 22 nm p-nc-SiO_X

Table 6.3: Different thicknesses of the p-layers tested in the TRJ. P3 is used in the a-SiGe/nc-Si tandem and P4 is used in the a-Si/a-SiGe tandem.

The results for the a-SiGe/nc-Si tandem are shown in Table 6.4. As the thickness is increased from 5 nm to 20 nm, both the V_{OC} and the fill factor improve. Beyond this point, these properties deteriorate. The fill factor using 20 nm is the highest even though it has the least current mismatch. This may be explained as follows. As the thickness increases, both the crystallinity and the amount of boron (irrespective of coordination) in the layer increase. These 2 effects may collectively lead to a

greater fraction of boron in 4-fold coordinated sites, which increases the hole density in the p-layer. This strengthens the electric field across the bottom junction and improves hole collection. Additionally, it is also possible that increasing the thickness of the p-doped layer improves hole selectivity [37]. The poor V_{OC} and fill factor of the cell deposited with a 25 nm p-layer in the TRJ may be because of the effect of counter doping. In tandem cells, the n-layer of the top junction is deposited immediately after the p-layer of the bottom junction. The hydrogen in the plasma may etch away some of the p-doped material. The resulting boron atoms in the plasma reduce the net donor concentration of the deposited n-layer, which results in a lower V_{OC} of the top subcell and poorer collection of electrons (which deteriorates fill factor). It is possible that, with a 25 nm thick p-layer, the deleterious effects of counter-doping outweigh the benefits of a thicker p-layer outlined above.

	Unit	5 nm	10 nm	15 nm	20 nm	25 nm
V_{OC}	mV	1113	1111	1138	1163	1144
J_{SC} a-SiGe	mA/cm^2	13.19	13.37	13.29	12.85	12.99
J_{SC} nc-Si	mA/cm^2	6.30	6.97	6.30	7.34	5.40
Fill factor	-	0.660	0.661	0.677	0.710	0.647
Efficiency	%	4.62	5.12	4.85	6.06	3.99

Table 6.4: Effect of varying the thickness of the p-layers used in the TRJ of the a-SiGe/nc-Si tandem.

For the a-Si/a-SiGe tandems, no overall trend was discernible in the V_{OC} and fill factor with increasing thickness (refer Table 6.5). However, the cell deposited with the 15 nm p-layer was found to have the highest V_{OC}, highest fill factor, and lowest series resistance. This may be because, at 15nm, there is a higher concentration of active dopants and better hole selectivity. This cannot be said with certainty, however, because the reduced series resistance may just be due to random variations in processing quality that occur from one deposition to the next. A trend was observed, however, in the current-matching of the tandem. As the thickness was increased, the current-matching was improved. This is likely the result of a thicker p-layer reflecting more light up into the a-Si subcell. However, this cannot be claimed with certainty in the absence of reflectance measurements.

	Unit	5 nm	10 nm	15 nm
V_{OC}	mV	1311	1322	1299
J_{SC} a-Si	mA/cm^2	7.06	7.74	8.27
J_{SC} a-SiGe	mA/cm^2	10.16	9.46	9.24
Fill factor	-	0.508	0.473	0.561

Table 6.5: Effect of varying the thickness of the p-layers used in the TRJ of the a-Si/a-SiGe tandem.

6.3. Optimization of n-doped layers

The different n-layers tested in the tandems are shown in Table D.6. The exact deposition conditions are provided in Appendix C. All the n-layers have an n-a-Si film at the i/n interface, except for N1 which has n-nc-SiO_X. This allows us to compare the effect of growing the top cell on a different substrate. Secondly, the phosphine gas flow for the n-layer at the n/p interface was reduced from N2 to N4. Finally, the n-layer at the n/p interface in N4 was deposited without any oxygen. Additional n-layers were also deposited, but their results could not be used because of processing errors. Nevertheless, the n-layers presented in Table D.6 allow some investigation into the role of oxygen at both the i/n and n/p interface, and the effect of doping. In the subsequent paragraphs, the effects of layers N1-N4 on both a-SiGe/nc-Si and a-Si/a-SiGe tandems are analysed simultaneously. The results are shown in Table 6.7.

Name	Composition
N1	25 nm n-nc-SiO_X 5 nm n-nc-SiO_X++
N2	25 nm n-a-Si 5 nm n-nc-SiO_X++
N3	25 nm n-a-Si 5 nm n-nc-SiO_X
N4	25 nm n-a-Si 5 nm n-nc-Si

Table 6.6: Different combinations of n-doped materials tested for use in the tunnel recombination junction.

Layer	a-Si/a-SiGe **V_{OC}**	a-Si/a-SiGe **Fill factor**	a-SiGe/nc-Si **V_{OC}**	a-SiGe/nc-Si **Fill factor**
-	mV	-	mV	-
N1	1297	0.427	1195	0.735
N2	1293	0.463	1201	0.741
N3	1292	0.416	1195	0.732
N4	1296	0.429	1198	0.741

Table 6.7: Results of using different combinations of n-layers in the TRJ of a-Si/a-SiGe and a-SiGe/nc-Si tandems.

For both tandems, using n-a-Si instead of n-nc-SiO_X at the i/n interface of the top junction appears to improve fill factor. It is hard to say why this is the case. Nevertheless, the reason might be that the the n-a-Si layer reduces the bandgap offset at the i/n interface [10], thus improving electron collection. However, N3 was found to have the worst fill factor for both tandems despite the n-a-Si layer at the i/n interface. This is possibly because of a couple of reasons. N3 is less doped than N2, which reduces the electric field across the top junction. This can reduce carrier collection and contribute to the low overall V_{OC}. Compared to N4, N3 arguably has lower crystallinity due to the presence of an amorphous silicon oxide phase. This leads to less active doping, which in turn reduces recombination at the n/p interface.

There is no single best performing n-layer among the tested combinations. However, 3 observations may be made. Firstly, the presence of n-a-Si contributes to an improved fill factor, likely due to a better i/n interface. Secondly, the presence of n-nc-Si at the n/p interface improves recombination of charge carriers. Thirdly, an n-nc-SiO_X layer be used to create a strong electric field across the top junction to improve the collection of charge carriers. An optimized n-layer may therefore be designed as such - n-a-Si at the i/n interface, n-nc-Si at the n/p interface, and n-SiO_X in between. To test this hypothesis, 2 sets of 8 n-layer combinations were processed, 1 for each tandem device. The experiment allowed for the study of the relative thicknesses of each layer, and the total n-layer thickness. Unfortunately, these cells could not be completed in time because the RF sputtering tool was out of order.

6.4. Conclusion

In summary, a systematic optimization of tunnel recombination junctions was pursued. The p-layer composition was varied. A highly doped p-nc-SiO_X layer at the n/p interface was found to work best for the a-SiGe/nc-Si tandem. For the a-Si/a-SiGe tandem, a thin p-nc-Si layer with low activation energy at the n/p interface was found to help. The thicknesses of these layers was varied next. A 20 nm p-stack in the TRJ of the a-SiGe/nc-Si tandem was found to be beneficial for V_{OC} and fill factor. In the case of the a-Si/a-SiGe device, current matching was observed to improve as the thickness was increased from 5 nm to 15 nm. This is possibly attributable to higher reflectance. After the optimization of the p-stack, different n-layers were tested. Although no single best performing n-layer was identified, some

insight into the role played by n-a-Si, n-nc-SiO_X, and n-nc-Si was obtained. A final experiment had been conducted to investigate the relative importance of these layers and thickness, but the devices could not be completed in time due to equipment failure.

7

Conclusions and recommendations

The properties of multijunction devices based on thin film silicon alloys make them uniquely suitable for certain applications. Important among these is the development of an integrated solar-to-fuel device, which may convert water and carbon dioxide into syn gas. The optimal design of multijunction devices is therefore an important area of study. This was the subject of this thesis. This was tackled in the form of 3 specific research objectives: development of high V_{OC} top junctions, flexible design of a-SiGe cells, and optimization of tunnel recombination junctions. The conclusions and recommendations emerging from the work done on each of these topics is presented below.

For the development of high V_{OC} top junctions, cells based on a-Si and a-SiO_X absorber layers were studied. High voltages of around 890 mV were obtained from both of these materials by varying the gas flows during PECVD. This was despite the fact that a-SiO_X has a wider bandgap than a-Si. Effectively, these observations give us the ability to change the spectrum over which the top junction absorbs light while maintaining the same V_{OC}. a-SiO_X based cells might be more useful in devices having 3 or more junctions because it allows more light to pass through to the underlying cells. The advantage of a-Si is that thinner absorber layers may be used to obtain the same current density and high V_{OC} values. Thinner absorber layers show reduced light-induced degradation. Thus, the study of a-Si and a-SiO_X based cells lead to the identification of some advantages of each material which may help in the process of multijunction device design.

The second research objective was related to the design of a-SiGe cells. a-SiGe cells are importance because their properties can be tuned to make them suitable for use in a variety of devices. A novel, semi-empirical approach to a-SiGe cell design was presented. a-SiGe absorber layers of profiled bandgaps were considered because of their versatility. The bandgap profile was divided into 3 variables: the layer thickness, the fraction of the layer deposited with minimum bandgap (i.e., plateau fraction), and the peak germane flow used during processing. Experiments were done to investigate the effects of varying each of these parameters while keeping the others constant. Subsequently, a set of semi-empirical equations were derived which approximately account for the effects of changing all three parameters. These equations were fitted to the measured data and subsequently used to visualize how changing more than one feature of the bandgap profile would affect device performance. As a result of this study, it was possible to draw a number of insights. Firstly, the equations helped to determine the different types of bandgap profile which would yield similar device performance for the studied cells. The advantage here is that, for a required current density, the bandgap profile which offers the highest V_{OC} may be chosen. This could improve the performance of the whole device. Secondly, and more interestingly, it was possible to control more nuanced aspects of a-SiGe cell performance. For instance, the presented method can indicate how to obtain the same current density from two a-SiGe cells but from different parts of the spectrum. Such insights can be quite useful for designing a-SiGe cells for use in different kinds of multijunction devices. It bears repeating here that the specific values of the J_{SC} and V_{OC} due to different bandgap profiles are highly dependent on a variety of deposition conditions. The key contribution in this respect is the approach itself - a method for expediently designing a-SiGe cells for versatile applications.

Finally, a systematic optimization of tunnel recombination junctions (TRJs) was attempted. Different features of the TRJ were varied: combinations of p-layers used, thicknesses of the p-layers, and the combinations of n-layers. These TRJs were deposited as part of both a-SiGe/nc-Si and a-Si/a-SiGe tandems. Due to the complexity of this task and experimental difficulties, it was difficult to identify the origin of the observed trends. Nonetheless, best performing p-layers and their thicknesses were identified for both sets of tandems. For the n-layers, no single best-performing combination could be identified. Nonetheless, the results hinted at different roles played by different n-layers in the TRJ. In light of this observation, it was suggested that an optimal combination of n-layers would include n-a-Si at the i/p interface, n-nc-Si at the n/p interface, and n-nc-SiO_X in between. 2 sets of 8 tandem devices each were processed to test this hypothesis, but they could not be completed in time because of equipment unavailability.

The work done as part of each research objective indicates ways in which multijunction devices may be designed better. Top junctions based on a-Si and a-SiO_X were studied, and their unique advantages identified. A novel design approach for a-SiGe junctions was presented, which can help with the customization of a-SiGe junctions for diverse applications. This was arguably the key contribution of this thesis. Finally, a systematic study of tunnel recombination junctions was conducted. Collectively, the results of this study may contribute to the better design of multijunction devices.

A GENPRO4 simulations of a-SiGe cells

A.1. Thickness series

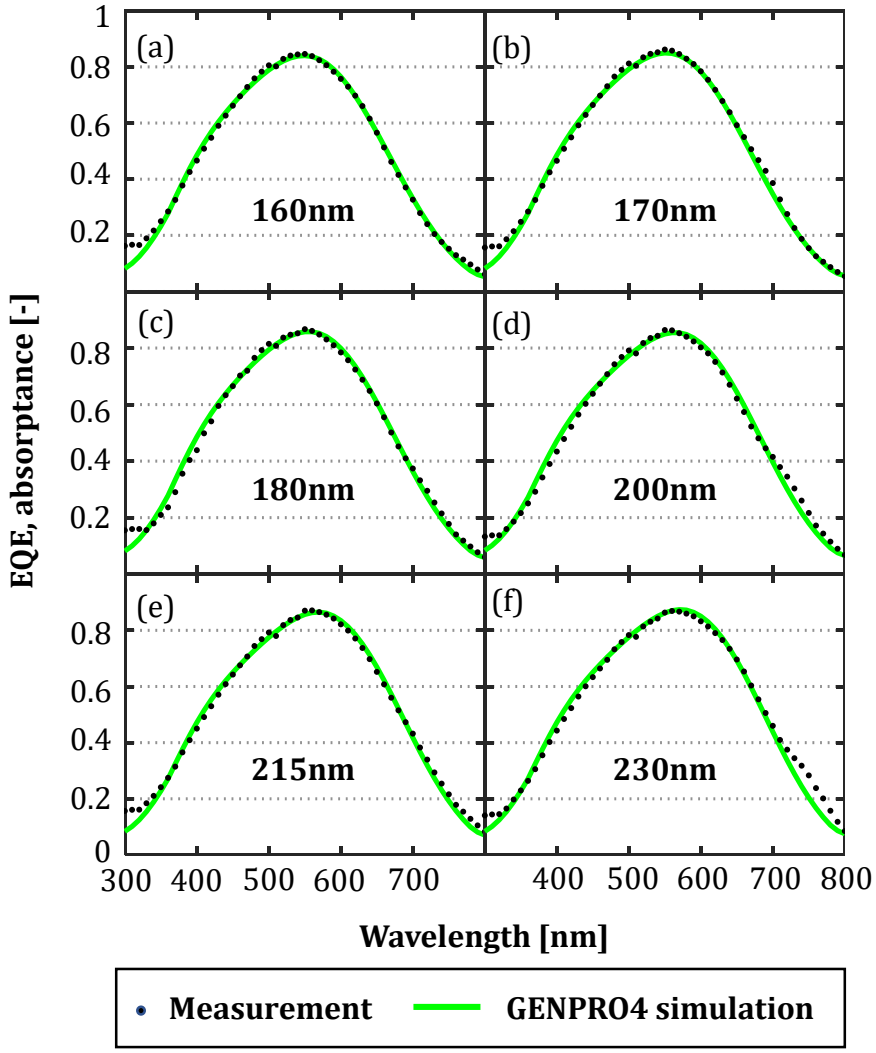

Figure A.1: GENPRO4 simulations of the a-SiGe cells of different thicknesses.

A.2. Plateau series

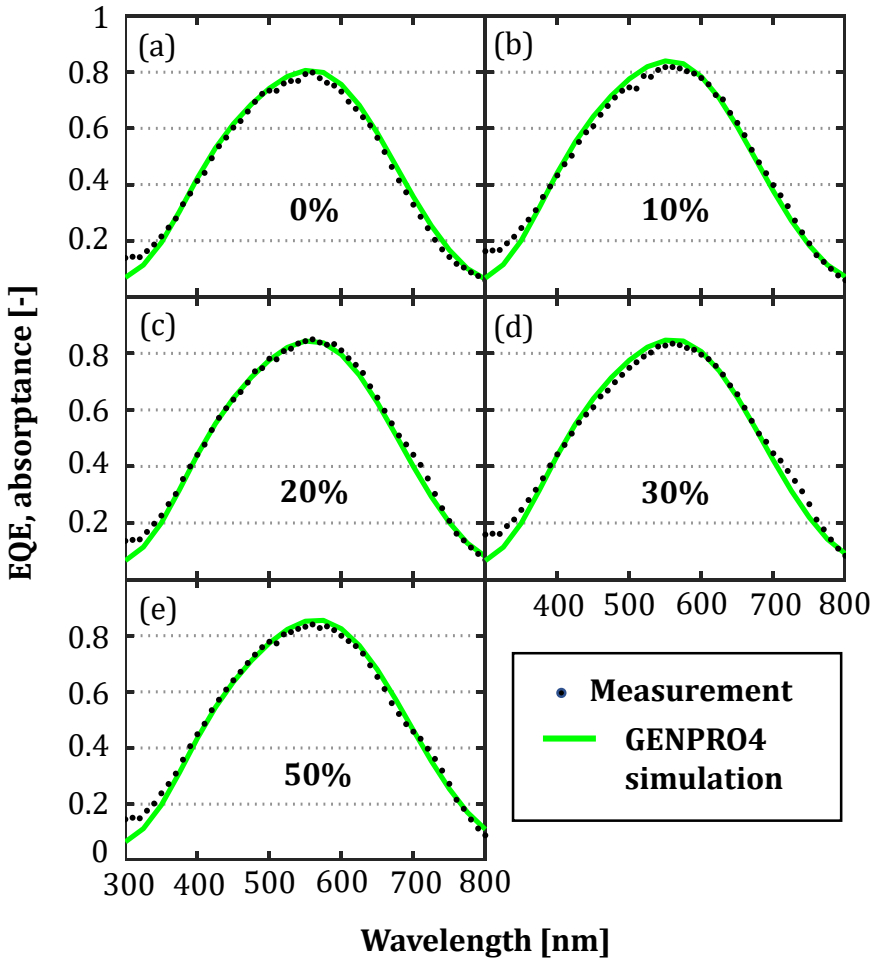

Figure A.2: GENPRO4 simulations of a-SiGe cells of different plateau fractions.

A.3. Peak germane flow series

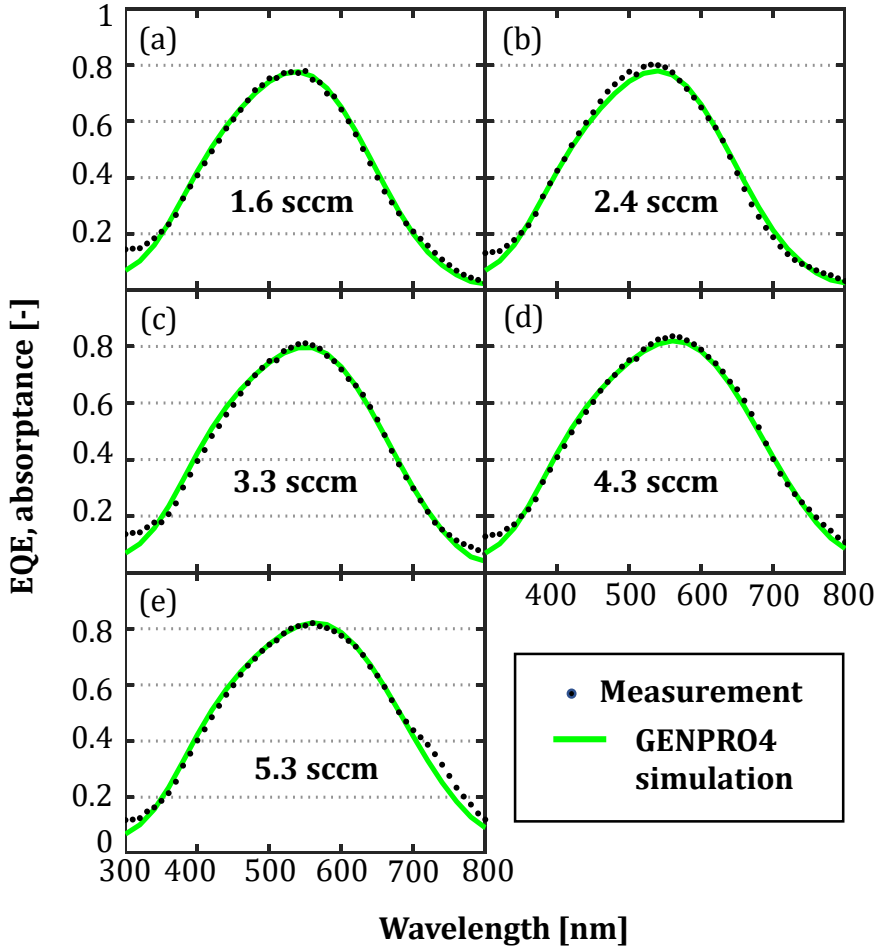

Figure A.3: GENPRO4 simulations of a-SiGe cells of different peak flows.

B

Relation between bandgap profile and cell parameters

This appendix presents the semi-empirical relationships used for analysing the impact of bandgap profiling on a-SiGe cells. First, the relationship is theoretically motivated. Then, the constants in the expression are fitted to experimental data using the Curve Fitting tool in MATLAB. Finally, the results of this fitting procedure are presented along with the goodness of fit values. This is first done for the J_{SC} and then the V_{OC}.

B.1. Bandgap profile and short-circuit current density

From Lambert-Beer's Law, the intensity of light decays exponentially inside an absorber.

$$I_x = I_0 exp(-\alpha x) \tag{B.1}$$

where I_0 is the intensity of the incident light, I_x is the intensity of light at a distance x inside the absorber, and α is the absorption coefficient. Intuitively, the photocurrent generated in the cell must be proportional to the attenuation in intensity of light as it passes through the absorber. Thus, for an absorber of thickness W,

$$J_{ph} \approx A\{1 - exp(-\alpha W)\} \tag{B.2}$$

where A is a constant. In a-SiGe cells with profiled bandgaps, the absorption coefficient changes along with width of the absorber. Consequently, the above expression cannot be directly applied in this case. For ease of analysis, the a-SiGe layer with a profiled bandgap is disaggregated into a stack of 3 layers of different bandgaps. These layers correspond to the i-p, plateau, and i-n regions. For simplicity, it is assumed that the absorption coefficient does not change appreciably across each of these layers. The photocurrents generated in each of these layers is then given by the following equations:

$$J_{ph,1} \approx A\{1 - exp(-\alpha_1 w_1)\} \tag{B.3}$$

$$J_{ph,2} \approx Aexp(-\alpha_1 w_1)\{1 - exp(-\alpha_2 w_2)\} \tag{B.4}$$

$$J_{ph,3} \approx Aexp(-\alpha_1 w_1 - \alpha_2 w_2)\{1 - exp(-\alpha_3 w_3)\} \tag{B.5}$$

where $\alpha_1, \alpha_2, \alpha_3$ represent the approximate absorption coefficients of the i-p region, plateau region, and i-n region respectively. The thicknesses of these regions are represented by w_1, w_2, and w_3 respectively. The total photocurrent from the absorber can be calculated by simply adding up the photocurrents from each layer. Furthermore, in the ideal case the photocurrent is the same as its short circuit current density. Thus,

$$J_{SC} \approx A\{1 - exp(-\alpha_1 w_1 - \alpha_2 w_2 - \alpha_3 w_3)\} \tag{B.6}$$

The fraction of the absorber constituting the plateau region is represented by Δw. The total thickness is W. The ratio of the i-p region width to the i-n region width is held constant at (say) r_w. Using these symbols, equation B.6 can be rewritten as

$$J_{SC} \approx A\{1 - exp(-\alpha_1 r_w W \frac{1-\Delta w}{1+r_w} - \alpha_2 W \Delta w - \alpha_3 W \frac{1-\Delta w}{1+r_w})\} \tag{B.7}$$

Rearranging the terms,

$$J_{SC} \approx A[1 - exp\{-\frac{\alpha_1 r_w}{1+r_w} W - (\alpha_2 - \frac{\alpha_1 r_w + \alpha_3}{1+r_w}) W \Delta w\}] \tag{B.8}$$

where the terms highlighted in blue can be considered constant for this study. Substituting the first constant term as B and the second one as C, the entire expression simplifies to

$$J_{SC} \approx A\{1 - exp(-BW - CW\Delta w\} \tag{B.9}$$

If the absorber thickness is increased to infinity, the J_{SC} becomes equal to A. Thus, A is a measure of all the photons that can possibly be absorbed by the layer. Theoretically, the total number of photons available for absorption are all the photons with energy higher than the minimum bandgap inside the material. Thus, A is likely to be a function of the minimum bandgap of the material.

The minimum bandgap determines the wavelength at which the layer can start absorption. The relation between these quantities is given by the following expression:

$$\lambda_{abs} = \frac{hc}{E_{min}} \approx \frac{1240}{E_{min}} \tag{B.10}$$

where E_{min} is the minimum optical bandgap inside the material and λ_{abs} is the wavelength at which absorption starts. Using the above equation, A can equivalently be described as a function of λ_{abs}. As this wavelength increases, additional photons become available for absorption. The number of additional photons available by a $\Delta\lambda$ shift in λ_{abs} can be estimated by looking at the AM1.5 spectrum in the relevant wavelength range. For a-SiGe cells, the wavelength range over which λ_{abs} may shift is 600-900nm. As shown in Figure B.1, the AM1.5 spectrum is approximately linear in this range.

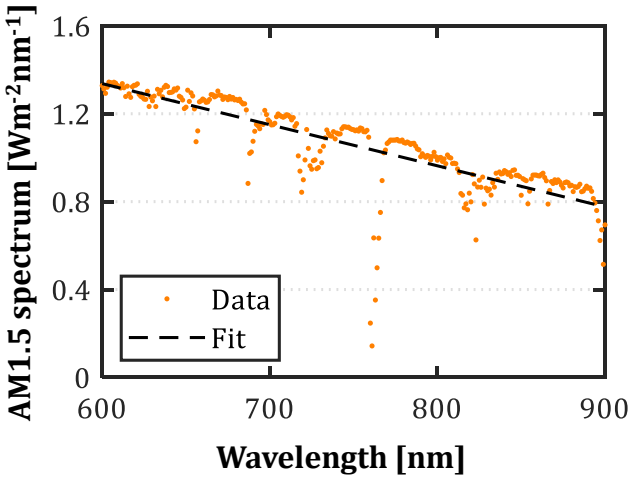

Figure B.1: The AM1.5 spectrum in the 600 - 800 nm wavelength range, and a linear approximation of its trend.

Mathematically, this means that the magnitude of increase in A decreases as λ_{abs} increases. In other terms,

$$\frac{dA}{d\lambda_{abs}} = -k_1 \lambda_{abs} + k_2 \tag{B.11}$$

where k_1, k_2 are constants. Integrating,

$$A = -k_1 {\lambda_{abs}}^2 + k_2 \lambda_{abs} + k_3 \tag{B.12}$$

Substituting λ_{abs} for E_{min} using equation,

$$A = -k_1 \left(\frac{1240}{E_{min}}\right)^2 + k_2 \frac{1240}{E_{min}} + k_3 \tag{B.13}$$

The minimum bandgap inside the absorber depends on the peak germane flow using during deposition. By measuring the optical bandgap of a-SiGe films deposited at different germane flows, a relationship between flow rate and bandgap was established. This relation was found to be approximately linear.

$$E_{04} = 1.86 - 0.0773 f_{GeH_4} \tag{B.14}$$

The minimum bandgap can then be equivalently expressed in terms of the maximum germane flow:

$$E_{min} = 1.86 - 0.0773 f_{peak} \tag{B.15}$$

In this way, A can be reduced to a function of the peak germane flow rate used during deposition. The short-circuit current density can now be expressed entirely in terms of the layer thickness, plateau fraction, and peak germane flow. Collectively, these variables define the bandgap profile. The complete expression for J_{SC} is given as:

$$J_{SC} \approx A(f_{peak})\{1 - exp(-BW - CW\Delta w\} \tag{B.16}$$

where

$$A(f_{peak}) \approx \frac{K_1}{(1.86 - 0.0773 f_{peak})^2} + \frac{K_2}{1.86 - 0.0773 f_{peak}} + K_3 \tag{B.17}$$

There are 5 constants in this equation: B, C, K_1, K_2, K_3. These constants were determined with the help of the experimental data. Experiments were done to investigate the role of each individual variable (thickness, plateau, and peak flow rate) on the cell performance while keeping the other variables constant. This was advantageous because it simplified the process of curve fitting. When only thickness is varied, equation reduces to a relatively simple Lambert-Beer law expression. For plateau fraction series, a similar equation needs to be fitted to the measurements. When only varying the germane flow, the exponential term in the equation can be considered constant and the equation assumes a polynomial form. In this way, the task of fitting a complicated equation to a vast set of data can be done by simultaneously fitting 3 relatively simpler equations to the measurements. The results of the fit are given in Figure B.2. The values of the constants thus obtained are shown in Table B.1.

Constant	Value
K_1	-149.1
K_2	222.7
K_3	-64.35
B	0.0119
C	0.01226

Table B.1: Values of constants in equations B.16 and B.17 obtained after fitting to experimental data.

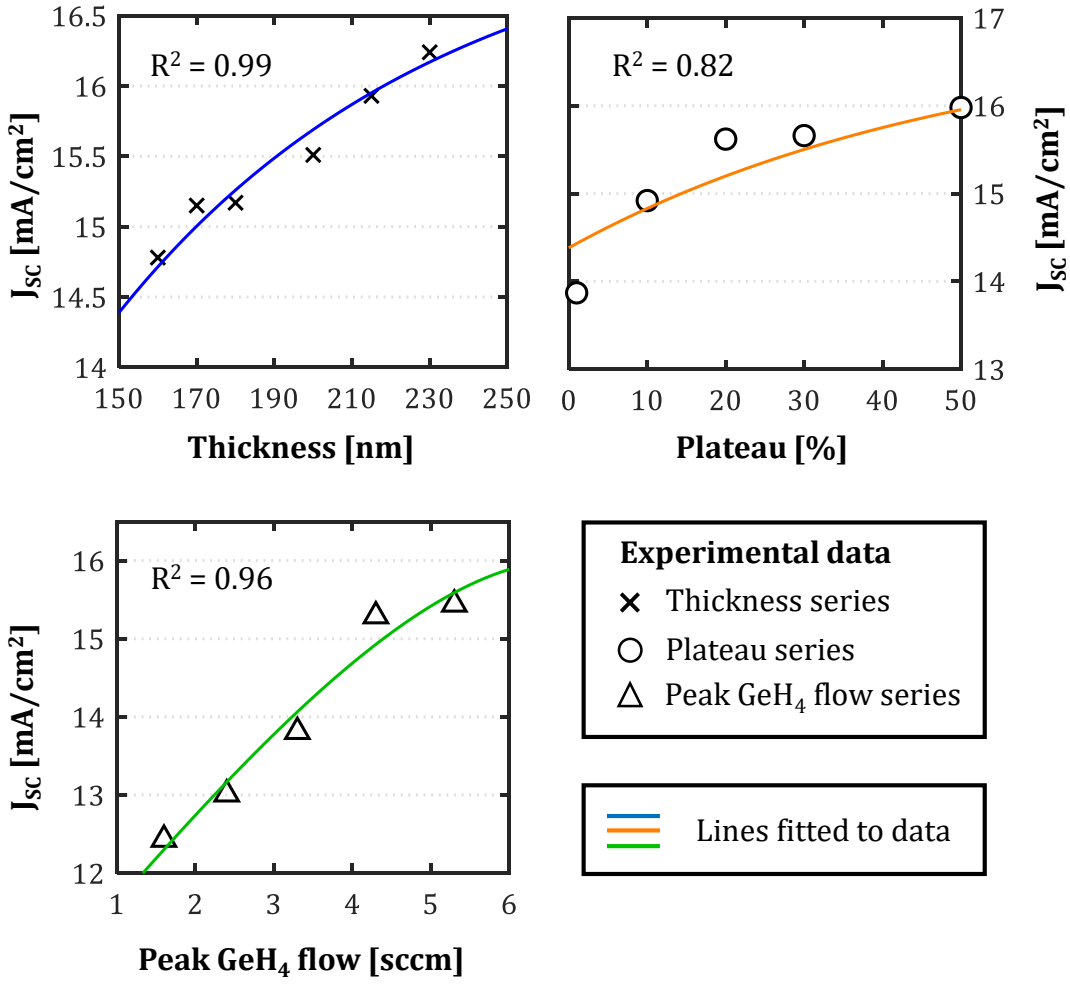

Figure B.2: Experimental data on the effect of thickness, plateau fraction, and peak germane flow on a-SiGe device J_{SC} and their respective fits.

B.2. Bandgap profile and open-circuit voltage

The V_{OC} of a drift device does not readily lend itself to straightforward analysis. Nonetheless, a good starting point is the following expression:

$$V_{OC} \approx \frac{nk_BT}{q} ln\left(\frac{J_{SC}}{J_0}\right) = \frac{nk_BT}{q}\{ln(J_{SC}) - ln(J_0)\} \tag{B.18}$$

where n is the ideality factor of the device, k_B is the Boltzmann constant, and T is the absolute temperature. J_0 is the saturation current density and is a measure of the amount of recombination in the device. The effect of bandgap profile on J_{SC} is known (refer previous section). Therefore, in order to study the effect of bandgap profile on V_{OC}, the relation between bandgap profile and J_0 must be described.

From [15],

$$J_0 = BT^{\gamma} exp\left(\frac{-E_g}{k_BT}\right) \tag{B.19}$$

where B is a constant which depends on the material properties of the material related to recombination, such a diffusion length. γ is another material property which describes the temperature depen-

dence of saturation current density. Since we are only investigating the performance of the device at constant temperature, this term can be considered constant.

Substituting the above expression into equation and replacing E_g by E_{04},

$$V_{OC} \approx \frac{nk_BT}{q}\left(ln(J_{SC}) - ln(B) - \gamma ln(T) + \frac{E_{04}}{k_BT}\right) \tag{B.20}$$

In our cells, the bandgap varies along with width of the absorber. Thus, it makes more sense to talk of an averaged bandgap $\overline{E_{04}}$ instead. This averaged bandgap can be calculated from the average germane flow rate by using Equation B.14. The averaged germane flow rate can be calculated as follows:

$$\overline{f_{GeH_4}} = \frac{1}{W}\int_W f_{GeH_4}dx \tag{B.21}$$

The germane flow rate varies linearly in the i-p and i-n regions, and remains constant in the plateau region. Let the maximum germane flow be f_{peak}. Assuming the minimum germane flow is 0, the above expression can be integrated piece-wise over the different regions of the absorber in a straightforward manner. The expression for averaged germane flow is then

$$\overline{f_{Geh_4}} = \frac{f_{peak}}{2}(1 + \Delta w) \tag{B.22}$$

Using equation B.14 and B.22, the averaged bandgap $\overline{E_{04}}$ can be expressed in terms of $f_{peak}, \Delta w$, and W. Substituting this directly into our expression for V_{OC},

$$V_{OC} \approx \frac{nk_BT}{q}\left\{ln(J_{SC}) - ln(B) - \gamma ln(T) + \frac{1.86}{k_BT} - \frac{0.0773}{2k_BT}f_{peak}\,(1 + \Delta w)\right\} \tag{B.23}$$

As mentioned previously, the parameter B in the above equation depends on the material properties of the layer. From equation B.19, it can be seen that larger values of B mean more recombination. It is quite challenging to accurately model recombination in thin film cells. However, one thing that can be said about recombination is that it increases in thicker absorber layers. In thicker a-SiGe layers, charge carriers encounter more defects which increases recombination. Thus, in simple terms, it may be said that B is directly proportional to thickness of the absorber layer W. Thus, our expression for V_{OC} now becomes

$$V_{OC} \approx \frac{nk_BT}{q}\left\{ln(J_{SC}) - ln(C_1) - ln(W) - \gamma ln(T) + \frac{1.86}{k_BT} - \frac{0.0773}{2k_BT}f_{peak}\,(1 + \Delta w)\right\} \tag{B.24}$$

Rearranging the terms,

$$V_{OC} \approx \frac{nk_BT}{q}ln\left(\frac{J_{SC}}{W}\right) - \frac{0.0773n}{2q}f_{peak}(1 + \Delta w) + \frac{nk_BT}{q}\left\{\frac{1.86}{k_BT} - ln(C_1) - \gamma ln(T)\right\} \tag{B.25}$$

The terms highlighted in blue are considered constant for the purposes for this study. Thus, the influence of bandgap profile on V_{OC} may be more simply expressed as

$$V_{OC} \approx Dln\left(\frac{J_{SC}}{W}\right) - Ef_{peak}(1 + \Delta w) + F \tag{B.26}$$

where J_{SC} in turn calculated using equation.

Using a similar strategy for fitting as described in the previous section, the values of the constants D, E, F were obtained. These are given in Table B.2. The results of the fitting process are shown in Figure B.3.

Constant	Value
D	52
E	35
F	910

Table B.2: Values of constants in equations B.26 obtained after fitting to experimental data

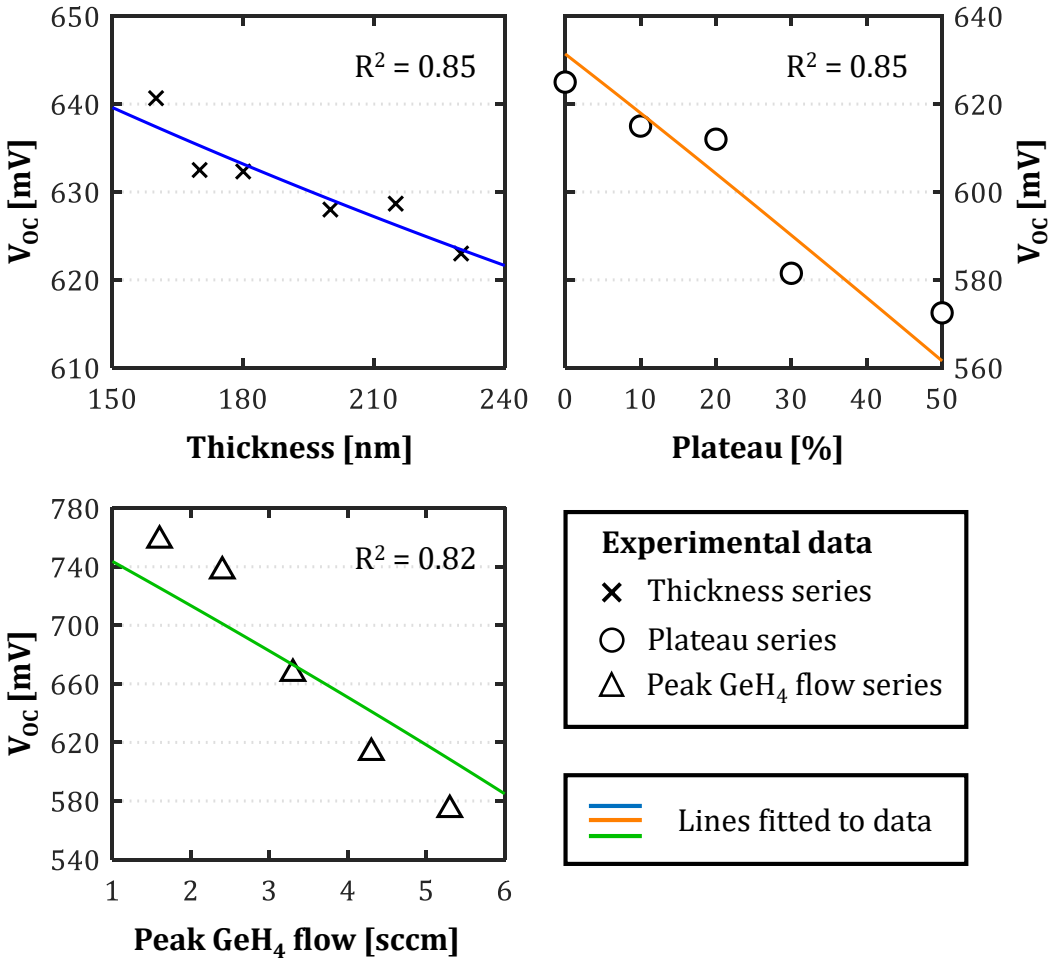

Figure B.3: Experimental data on the effect of thickness, plateau fraction, and peak germane flow on a-SiGe device V_{OC} and their respective fits.

C

PECVD processing conditions of thin films

C.1. P-doped films used in tunnel recombination junctions

Layer	SiH_4	B_2H_6 (200ppm in H_2)	CO_2	H_2	Pressure	Power
-	sccm	sccm	sccm	sccm	mbar	W
p-nc-SiO_X	0.8	10	2.2	170	2.2	12
p-nc-SiO_X+	0.8	30	2.2	170	2.2	12
p-nc-SiO_X++	0.8	50	2.2	170	2.2	12
p-nc-Si_{low}	0.6	32	0	200	2.2	12
p-nc-$Si_{35\ W}$	0.8	40	0	170	2.2	35

Table C.1: Deposition parameters of the different p-doped layers used in tunnel recombination junctions.

C.2. N-doped films used in the tunnel recombination junctions

Layer	SiH_4	PH_3	CO_2	H_2	Pressure	Power
-	sccm	sccm	sccm	sccm	mbar	W
n-nc-SiO_X	1	2	1.6	120	1.5	11
n-nc-SiO_X+	1	3	1.6	120	1.5	11
n-nc-SiO_X++	1	3.6	1.6	120	1.5	11
n-nc-Si	1	2	120	0	1.5	11
n-a-Si	40	11	0	0	0.6	4

Table C.2: Deposition parameters of the different n-doped layers used in tunnel recombination junctions.

D

Measurements of tandem device performance

D.1. Tandems deposited with different p-layers in the TRJ

Name	Composition
P1	12 nm p-nc-SiO_X
P2	6 nm p-nc-SiO_X+ 6 nm p-nc-SiO_X
P3	6 nm p-nc-SiO_X++ 6 nm p-nc-SiO_X
P4	3 nm p-nc-Si_{low} 9 nm p-nc-SiO_X
P5	3 nm p-nc-$Si_{35\ W}$ 9 nm p-nc-SiO_X

Table D.1: Different combinations of p-type materials investigated for use in TRJ.

	Units	P1	P2	P3	P4	P5
V_{OC}	mV	1113	1114	1112	1120	1110
J_{SC} a-SiGe	mA/cm^2	15.69	15.36	15.17	15.17	14.74
J_{SC} nc-Si	mA/cm^2	5.47	5.60	5.68	5.45	6.11
R_S	Ωm^2	17.01	12.70	13.39	12.65	14.52
R_{sh}	Ωm^2	13294.29	13742.65	16071.68	6723.30	7982.58
Fill factor	-	0.707	0.717	0.725	0.668	0.687
Efficiency	%	4.30	4.47	4.58	4.08	4.66

Table D.2: Effect of varying the combination of p-layers in the TRJ in a-SiGe/nc-Si tandems.

	Units	P1	P2	P3	P4	P5
V_{OC}	mV	1272	1369	1348	1382	1378
J_{SC} a-Si	mA/cm^2	8.90	9.68	9.09	9.51	9.71
J_{SC} a-SiGe	mA/cm^2	4.96	5.42	5.49	6.41	5.63
R_S	Ωm^2	119.06	56.12	40.54	27.69	40.76
R_{sh}	Ωm^2	5597.42	8207.28	9969.34	12269.99	12318.85
Fill factor	-	0.325	0.435	0.479	0.576	0.539
Efficiency	%	2.05	3.23	3.55	5.10	4.18

Table D.3: Effect of varying the combination of p-layers in the TRJ in a-Si/a-SiGe tandems.

	Units	5 nm	10 nm	15 nm	20 nm	25 nm
V_{OC}	mV	1113	1111	1138	1163	1144
J_{SC} a-SiGe	mA/cm^2	13.19	13.37	13.29	12.85	12.99
J_{SC} nc-Si	mA/cm^2	6.30	6.97	6.30	7.34	5.40
R_S	Ωm^2	59.56	106.69	40.94	15.02	14.79
R_{sh}	Ωm^2	7586.47	9582.54	9073.18	11210.21	9730.66
Fill factor	-	0.660	0.661	0.677	0.710	0.647
Efficiency	%	4.62	5.12	4.85	6.06	3.99

Table D.4: Effect of varying the thickness of p-layers at the TRJ in a-SiGe/nc-Si tandems.

	Units	5 nm	10 nm	15 nm	20 nm	25 nm
V_{OC}	mV	1311	1322	1299	1060	1280
J_{SC} a-Si	mA/cm^2	7.06	7.74	8.27	6.67	2.88
J_{SC} a-SiGe	mA/cm^2	10.16	9.46	9.24	9.54	10.64
R_S	Ωm^2	38.02	39.43	26.38	36.78	39.00
R_{sh}	Ωm^2	9641.99	7617.64	9734.44	2481.92	20089.42
Fill factor	-	0.508	0.473	0.561	0.39	0.65
Efficiency	%	4.70	4.84	6.03	2.78	2.38

Table D.5: Effect of varying the thickness of p-layers in the TRJ in a-Si/a-SiGe tandems.

D.2. Tandems deposited with different n-layers in the TRJ

Name	Composition
N1	25 nm n-nc-SiO_X 5 nm n-nc-SiO_X++
N2	25 nm n-a-Si 5 nm n-nc-SiO_X++
N3	25 nm n-a-Si 5 nm n-nc-SiO_X
N4	25 nm n-a-Si 5 nm n-nc-Si
N5	4 nm n-a-Si 8.5 nm n-nc-SiO_X 8.6 nm n-nc-SiO_{X2} 9 nm n-nc-Si
N6	25 nm n-nc-SiO_X 5 nm n-nc-Si
N7	25 nm n-nc-SiO_X 5 nm n-nc-Si

Table D.6: Different combinations of n-doped materials tested for use in the tunnel recombination junction.

	Units	N1	N2	N3	N4	N5	N7
V_{OC}	mV	1195	1201	1195	1198	1208	1095
J_{SC} a-SiGe	mA/cm^2	10.02	10.30	10.38	9.77	10.49	25.25
J_{SC} nc-Si	mA/cm^2	6.47	6.40	6.37	6.46	6.53	8.63
R_S	Ωm^2	17.22	15.43	15.83	13.31	14.74	13.07
R_{sh}	Ωm^2	18276.71	17918.32	17346.78	19482.21	9323.96	26483.75
Fill factor	-	0.735	0.741	0.732	0.741	0.705	0.696
Efficiency	%	5.68	5.69	5.58	5.73	5.56	1.93

Table D.7: Effect of varying the combination of n-layers at the TRJ in a-SiGe/nc-Si tandems.

	Units	N1	N2	N3	N4	N6	N7
V_{OC}	mV	1297	1293	1292	1296	1294	1310
J_{SC} a-Si	mA/cm^2	8.94	9.38	9.62	9.86	6.75	6.92
J_{SC} a-SiGe	mA/cm^2	9.20	8.33	8.05	8.08	10.34	11.01
R_S	Ωm^2	26.44	26.68	30.38	31.07	32.81	34.55
R_{sh}	Ωm^2	3645.87	3933.10	3025.31	2848.04	6839.39	8147.03
Fill factor	-	0.427	0.463	0.416	0.429	0.480	0.485
Efficiency	%	4.95	4.98	4.33	4.50	4.20	4.40

Table D.8: Effect of varying the combination of n-layers at the TRJ in a-Si/a-SiGe tandems.

Bibliography

[1] Ashish Binani. Optimizing the p-contact of an nip substrate solar cell. Master's thesis, Delft University of Technology, 2019.

[2] Grégory Bugnon, Gaetano Parascandolo, Thomas Söderström, Peter Cuony, Matthieu Despeisse, Simon Hänni, Jakub Holovskỳ, Fanny Meillaud, and Christophe Ballif. A new view of microcrystalline silicon: the role of plasma processing in achieving a dense and stable absorber material for photovoltaic applications. *Advanced Functional Materials*, 22(17):3665–3671, 2012.

[3] Debajyoti Das, SM Iftiquar, and AK Barua. Wide optical-gap a-sio: H films prepared by rf glow discharge. *Journal of non-crystalline solids*, 210(2-3):148–154, 1997.

[4] Xunming Deng, Xianbo Liao, Sijin Han, Henry Povolny, and Pratima Agarwal. Amorphous silicon and silicon germanium materials for high-efficiency triple-junction solar cells. *Solar Energy Materials and Solar Cells*, 62(1-2):89–95, 2000.

[5] Qi Hua Fan, Changyong Chen, Xianbo Liao, Xianbi Xiang, Shibin Zhang, William Ingler, Nirupama Adiga, Zhihua Hu, Xinmin Cao, Wenhui Du, et al. High efficiency silicon–germanium thin film solar cells using graded absorber layer. *Solar Energy Materials and Solar Cells*, 94(7):1300–1302, 2010.

[6] Marinus Fischer, Hairen Tan, Jimmy Melskens, Ravi Vasudevan, Miro Zeman, and Arno HM Smets. High pressure processing of hydrogenated amorphous silicon solar cells: Relation between nanostructure and high open-circuit voltage. *Applied Physics Letters*, 106(4):043905, 2015.

[7] Yuan Gao, Fai Tong Si, Olindo Isabella, Rudi Santbergen, Guangtao Yang, Jianfei Dong, Guoqi Zhang, and Miro Zeman. Performance optimization of semi-transparent thin-film amorphous silicon solar cells. In *2017 IEEE 44th Photovoltaic Specialist Conference (PVSC)*, pages 2605–2609. IEEE, 2017.

[8] S Guha, J Yang, A Pawlikiewicz, T Glatfelter, R Ross, and SR Ovshinsky. Band-gap profiling for improving the efficiency of amorphous silicon alloy solar cells. *Applied Physics Letters*, 54(23): 2330–2332, 1989.

[9] Subhendu Guha, Jeffrey Yang, Arindam Banerjee, Baojie Yan, and Kenneth Lord. High quality amorphous silicon materials and cells grown with hydrogen dilution. *Solar energy materials and solar cells*, 78(1-4):329–347, 2003.

[10] Li Gui-Jun, Hou Guo-Fu, Han Xiao-Yan, Yuan Yu-Jie, Wei Chang-Chun, Sun Jian, Zhao Yin, and Geng Xin-Hua. The study of a new n/p tunnel recombination junction and its application in a-si: H/μc-si: H tandem solar cells. *Chinese Physics B*, 18(4):1674, 2009.

[11] Hou Guo-Fu, Xue Jun-Ming, Guo Qun-Chao, Sun Jian, Zhao Ying, Geng Xin-Hua, and Li Yi-Gang. Formation mechanism of incubation layers in the initial stage of microcrystalline silicon growth by pecvd. *Chinese Physics*, 16(2):553, 2007.

[12] Andrea Ingenito, Olindo Isabella, Serge Solntsev, and Miro Zeman. Accurate opto-electrical modeling of multi-crystalline silicon wafer-based solar cells. *Solar energy materials and solar cells*, 123:17–29, 2014.

[13] Sorapong Inthisang, Kobsak Sriprapha, Shinsuke Miyajima, Akira Yamada, and Makoto Konagai. Hydrogenated amorphous silicon oxide solar cells fabricated near the phase transition between amorphous and microcrystalline structures. *Japanese journal of applied physics*, 48(12R):122402, 2009.

[14] Sorapong Inthisang, Taweewat Krajangsang, Ihsanul Afdi Yunaz, Akira Yamada, Makoto Konagai, and Christopher R Wronski. Fabrication of high open-circuit voltage a-si1–xox: H solar cells by using p-a-si1–xox: H as window layer. *physica status solidi c*, 8(10):2990–2993, 2011.

[15] Klaus-Dieter Jäger, Olindo Isabella, Arno HM Smets, René ACMM van Swaaij, and Miro Zeman. *Solar energy: fundamentals, technology and systems*. UIT Cambridge, 2016.

[16] Chase Jenny. *Solar Power Finance Without the Jargon*. World Scientific, 2019.

[17] Do Yun Kim, Erwin Guijt, Fai Tong Si, Rudi Santbergen, Jakub Holovskỳ, Olindo Isabella, René ACMM van Swaaij, and Miro Zeman. Fabrication of double-and triple-junction solar cells with hydrogenated amorphous silicon oxide (a-siox: H) top cell. *Solar Energy Materials and Solar Cells*, 141:148–153, 2015.

[18] Do Yun Kim, Erwin Guijt, René ACMM van Swaaij, and Miro Zeman. Development of a-siox: H solar cells with very high voc× ff product. *Progress in Photovoltaics: Research and Applications*, 23(6):671–684, 2015.

[19] Do Yun Kim, Erwin Guijt, René ACMM van Swaaij, and Miro Zeman. Hydrogenated amorphous silicon oxide (a-sio x: H) single junction solar cell with 8.8% initial efficiency by reducing parasitic absorptions. *Journal of Applied Physics*, 121(13):133103, 2017.

[20] Soohyun Kim, Jin-Won Chung, Hyun Lee, Jinhee Park, Younho Heo, and Heon-Min Lee. Remarkable progress in thin-film silicon solar cells using high-efficiency triple-junction technology. *Solar Energy Materials and Solar Cells*, 119:26–35, 2013.

[21] Makoto Konagai. Present status and future prospects of silicon thin-film solar cells. *Japanese Journal of Applied Physics*, 50(3R):030001, 2011.

[22] National Renewable Energy Laboratory. Best research-cell efficiency chart, 2020. URL `https://www.nrel.gov/pv/cell-efficiency.html`.

[23] Aart Lagendijk, Bart Van Tiggelen, and Diederik S Wiersma. Fifty years of anderson localization. *Phys. Today*, 62(8):24–29, 2009.

[24] A Lambertz, F Finger, B Holländer, JK Rath, and REI Schropp. Boron-doped hydrogenated microcrystalline silicon oxide (μc-siox: H) for application in thin-film silicon solar cells. *Journal of Non-Crystalline Solids*, 358(17):1962–1965, 2012.

[25] N Layadi, P Roca i Cabarrocas, B Drévillon, and I Solomon. Real-time spectroscopic ellipsometry study of the growth of amorphous and microcrystalline silicon thin films prepared by alternating silicon deposition and hydrogen plasma treatment. *Physical Review B*, 52(7):5136, 1995.

[26] Jimmy Melskens, Arno HM Smets, Marc Schouten, Stephan WH Eijt, Henk Schut, and Miro Zeman. New insights in the nanostructure and defect states of hydrogenated amorphous silicon obtained by annealing. In *2012 IEEE 38th Photovoltaic Specialists Conference (PVSC) PART 2*, pages 1–8. IEEE, 2012.

[27] Andrew Michelmore, Jason D Whittle, and Robert D Short. The importance of ions in low pressure pecvd plasmas. *Frontiers in Physics*, 3:3, 2015.

[28] Shi Mingji, Wang Zhanguo, Liu Shiyong, Peng Wenbo, Xiao Haibo, and Zeng Xiangbo. Boron-doped silicon film as a recombination layer in the tunnel junction of a tandem solar cell. *Journal of Semiconductors*, 30(6):063001, 2009.

[29] Kenjiro Nakamura, Kunihiko Yoshino, Shinya Takeoka, and Isamu Shimizu. Roles of atomic hydrogen in chemical annealing. *Japanese Journal of Applied Physics*, 34(2R):442, 1995.

[30] Donald A Neamen. *Semiconductor physics and devices: basic principles*. New York, NY: McGraw-Hill„ 2012.

[31] Jian Ni, Jianjun Zhang, Yu Cao, Xianbao Wang, Xinliang Chen, Xinhua Geng, and Ying Zhao. Low temperature deposition of high open-circuit voltage (> 1.0 v) p–i–n type amorphous silicon solar cells. *Solar energy materials and solar cells*, 95(7):1922–1926, 2011.

[32] Katsuhiko Nomoto, Yuichi Urano, Jean Luc Guizot, Gautam Ganguly, and Akihisa Matsuda. Role of hydrogen atoms in the formation process of hydrogenated microcrystalline silicon. *Japanese journal of applied physics*, 29(8A):L1372, 1990.

[33] World Health Organization. Covid-19 intensifies the urgency to expand sustainable energy solutions worldwide, 2020. URL `https://bit.ly/2TSdDnI`.

[34] Joshua M Pearce, Randy J Koval, Andre S Ferlauto, Robert W Collins, Christopher R Wronski, Jeffrey Yang, and Subbhendu Guha. Dependence of open-circuit voltage in hydrogenated protocrystalline silicon solar cells on carrier recombination in p/i interface and bulk regions. *Applied Physics Letters*, 77(19):3093–3095, 2000.

[35] Bart Elger Pieters. *Characterization of thin-film silicon materials and solar cells through numerical modelling*. PhD thesis, Delft University of Technology, 2008.

[36] Jef Poortmans and Vladimir Arkhipov. *Thin film solar cells: fabrication, characterization and applications*, volume 5. John Wiley & Sons, 2006.

[37] Paul Procel, Guangtao Yang, Olindo Isabella, and Miro Zeman. Theoretical evaluation of contact stack for high efficiency ibc-shj solar cells. *Solar Energy Materials and Solar Cells*, 186:66–77, 2018.

[38] IEA PVPS. Snapshot of global pv markets. 2020.

[39] Carl Sagan. *Pale blue dot: A vision of the human future in space*. Random House Digital, Inc., 1997.

[40] Rudi Santbergen and RJ Ch van Zolingen. The absorption factor of crystalline silicon pv cells: A numerical and experimental study. *Solar energy materials and solar cells*, 92(4):432–444, 2008.

[41] Rudi Santbergen, Arno HM Smets, and Miro Zeman. Optical model for multilayer structures with coherent, partly coherent and incoherent layers. *Optics express*, 21(102):A262–A267, 2013.

[42] Rudi Santbergen, Tomomi Meguro, Takashi Suezaki, Gensuke Koizumi, Kenji Yamamoto, and Miro Zeman. Genpro4 optical model for solar cell simulation and its application to multijunction solar cells. *IEEE journal of photovoltaics*, 7(3):919–926, 2017.

[43] Jan-Willem Schuettauf, Bjoern Niesen, Linus Löfgren, Maximilien Bonnet-Eymard, Michael Stuckelberger, Simon Hänni, Mathieu Boccard, Grégory Bugnon, Matthieu Despeisse, Franz-Josef Haug, et al. Amorphous silicon–germanium for triple and quadruple junction thin-film silicon based solar cells. *Solar Energy Materials and Solar Cells*, 133:163–169, 2015.

[44] Fai Tong Si, Do Yun Kim, Rudi Santbergen, Hairen Tan, René ACMM van Swaaij, Arno HM Smets, Olindo Isabella, and Miro Zeman. Quadruple-junction thin-film silicon-based solar cells with high open-circuit voltage. *Applied Physics Letters*, 105(6):063902, 2014.

[45] Fai Tong Si, Olindo Isabella, Hairen Tan, and Miro Zeman. Quadruple-junction thin-film silicon solar cells using four different absorber materials. *Solar RRL*, 1(3-4):1700036, 2017.

[46] M Singh, R Santbergen, L Mazzarella, A Madrampazakis, G Yang, R Vismara, Z Remes, A Weeber, M Zeman, and O Isabella. Optical characterization of poly-siox and poly-sicx carrier-selective passivating contacts. *Solar Energy Materials and Solar Cells*, 210:110507, 2020.

[47] Jaran Sritharathikhun, Sorapong Inthisang, Taweewat Krajangsang, Amornrat Limmanee, and Kobsak Sriprapha. Optimization of an ia-siox: H absorber layer for thin film silicon solar cell applications. *Thin Solid Films*, 546:383–386, 2013.

[48] RL Stolk, H Li, RH Franken, JWA Schüttauf, CHM van der Werf, JK Rath, and REI Schropp. Improvement of the efficiency of triple junction n–i–p solar cells with hot-wire cvd proto-and micro-crystalline silicon absorber layers. *Thin Solid Films*, 516(5):736–739, 2008.

[49] Hairen Tan, Rudi Santbergen, Arno HM Smets, and Miro Zeman. Plasmonic light trapping in thin-film silicon solar cells with improved self-assembled silver nanoparticles. *Nano letters*, 12(8): 4070–4076, 2012.

[50] CC Tsai, GB Anderson, R Thompson, and B Wacker. Control of silicon network structure in plasma deposition. *Journal of Non-Crystalline Solids*, 114:151–153, 1989.

[51] K Winer, RA Street, NM Johnson, and J Walker. Impurity incorporation and doping efficiency in a-si: H. *Physical Review B*, 42(5):3120, 1990.

[52] Baojie Yan, Guozhen Yue, Jeffrey Yang, and Subhendu Guha. Correlation of current mismatch and fill factor in amorphous and nanocrystalline silicon based high efficiency multi-junction solar cells. In *2008 33rd IEEE Photovoltaic Specialists Conference*, pages 1–6. IEEE, 2008.

[53] Jeffrey Yang, Baojie Yan, and Subhendu Guha. Amorphous and nanocrystalline silicon-based multi-junction solar cells. *Thin Solid Films*, 487(1-2):162–169, 2005.

[54] Ihsanul Afdi Yunaz, Akira Yamada, and Makoto Konagai. Theoretical analysis of amorphous silicon alloy based triple junction solar cells. *Japanese Journal of Applied Physics*, 46(12L):L1152, 2007.

[55] M Zeman, O Isabella, S Solntsev, and K Jäger. Modelling of thin-film silicon solar cells. *Solar Energy Materials and Solar Cells*, 119:94–111, 2013.

[56] XX Zheng, XD Zhang, SS Yang, SZ Xu, CC Wei, and Y Zhao. Effect of the n/p tunnel junction on the performance of a-si: H/a-si: H/μc-si: H triple-junction solar cells. *Solar energy materials and solar cells*, 101:15–21, 2012.

[57] J Zimmer, Helmut Stiebig, and H Wagner. a-sige: H based solar cells with graded absorption layer. *Journal of applied physics*, 84(1):611–617, 1998.